Crystal structure and activity profiling of deubiquitinating inhibitors-bound to SARS-CoV-2 papain like protease revealed new allosteric sites for antiviral therapies

Shweta Choudhary[1], Sanketkumar Nehul[1], Santhosh Kambaiah Nagaraj[4], Rohan Narayan[4], Shalja Verma[1], Swati Sharma[1,2], Annu Kumari[1], Ruchi Rani[1], Ankita Saha[1], Debabrata Sircar[1], Shashank Tripathi[4], Gaurav Kumar Sharma[3*], Pravindra Kumar[1*], Shailly Tomar[1*]

[1]Department of Biosciences and Bioengineering, Indian Institute of Technology Roorkee, Uttarakhand (247667), India.
[2]Shiv Nadar University, Uttar Pradesh, (201314), India
[3]Indian Veterinary Research Institute, Izatnagar, Bareilly, Uttar Pradesh (243122), India
[4]Indian Institute of Science, Bangalore, India

***Corresponding author details**

Shailly Tomar
Professor,
Department of Biosciences and Bioengineering,
Indian Institute of Technology Roorkee,
Uttarakhand, India 247667
Tel: +91-1332-285849
Fax: 91-1332-273560
Email: shailly.tomar@bt.iitr.ac.in
ORCID ID: 0000-0002-1730-003X

Pravindra Kumar
Professor,
Department of Biosciences and Bioengineering,
Indian Institute of Technology Roorkee,
Uttarakhand, India 247667
E-mail: pravindra.kumar@bt.iitr.ac.in
Telephone: +91-1332-286286
ORCID ID: 0000-0003-2128-7736

Gaurav Kumar Sharma
Senior scientist,
Centre for Animal Disease Research and Diagnosis (CADRAD),
Indian veterinary Research Institute, Bareilly (IVRI, Bareilly)
Uttar Pradesh, India
Telephone: 0581-2302188
Email: gaurvet@gmail.com
ORCID ID: 0000-0002-9996-9422

Abstract

Emerging variants of SARS-CoV-2 still threaten the effectiveness of currently deployed vaccines, and antivirals can prove to be an effective therapeutic option for attenuating it. The papain-like protease (PLpro) is an attractive target due to its sequence conservation and critical role in the replication and pathogenesis of SARS-CoV-2. PLpro also plays very important role in modulation of host immune responses by deubiquitinating (DUBs) or deISGylating host proteins. Thus, targeting PLpro serves as a two-pronged approach to abate SARS-CoV-2. Due to its structural and functional similarities with the host DUB enzymes, an *in-house* library of DUB inhibitors was constituted in this study. Five promising compounds exhibiting high binding affinities with the substrate binding site of PLpro were identified from a library of 81 compounds with *in silico* screening, docking, and simulation studies. Interestingly, lithocholic acid, linagliptin, teneligliptin, and flupenthixol significantly inhibited the proteolytic activity of PLpro. Each of these compounds abrogated *in vitro* replication of SARS-CoV-2 with EC_{50} values in low micromolar range, when tested in Vero cells, HEK293T-ACE2, and A549-ACE2 cells. In addition, crystal structure of SARS-CoV-2 PLpro and its complex with inhibitors have been determined that revealed their inhibitory mechanism. The findings of this study provide the proof-of-principle that the DUB inhibitors hold high potential as a new class of therapeutics against SARS-CoV-2. Additionally, this is the first study that has opened a new avenue towards not only targeting PLpro active site but also simultaneously directing towards restoration of antiviral immune response of the host for deterring SARS-CoV-2.

Introduction

The pandemic of COVID-19, caused by the SARS-CoV-2 and the resurgence of drug resistant variants, has taken a heavy toll on global health and calls for effective and safe anti-SARS-CoV-2 drugs. The rapid rollout of vaccine-based prophylactic therapies against SARS-CoV-2 initially saved numerous lives but the resulting immune pressures from vaccinations and infections led to emergence of highly contagious immune escape variants [1][2]. Concerns have been raised about the diminishing range, strength, and duration of vaccinal as well as natural immunity, which could jeopardize the geographical or temporal efficacy of these interventions and could lead to breakthrough infections [1][3][4][5][6][7][8].

A number of small molecule therapeutics have been developed targeting the highly conserved viral proteins, aiming to limit the spread of SARS-CoV-2 infections. Precedent studies on SARS-CoV-2 highlight that the catalytic site of certain non-structural proteins (nsP) of SARS-CoV-2, such as papain-like protease (PLpro), 3-chymotrypsin-like protease (3CL pro or Mpro), RNA-dependent RNA polymerase (RdRp), and helicase display high levels of sequence similarity with their corresponding SARS and MERS counterparts and represent attractive antiviral targets against SARS-CoV-2 [9][10][11][12]. Furthermore, due to the high degree of conservation of these nsPs among other coronaviruses, the probability of emergence of new mutations in these proteins is presumably low compared to the spike protein of SARS-CoV-2 [13]. Examples of the FDA approved direct-acting antivirals include Remdesivir, which inhibits SARS-CoV-2 RdRp, and Paxlovid, which targets the main protease [9][14][15][16][17]. Nevertheless, resistant mutant SARS-CoV-2 strains against remdesivir and Paxlovid have been detected in cell culture and drug treated COVID-19 patients, raising a demand for additional antivirals with alternative modes of action to combat the drug-resistant and other SARS-CoV-2 variants [18], [19], [20], [21]. PLpro presents to be a more challenging and potentially promising druggable target of SARS-CoV-2, for which effective inhibitors are yet to be discovered [22].

The genome of SARS-CoV-2 comprises a single-stranded positive-sense RNA of ~ 30kb, which is translated to produce structural, non-structural, and accessory viral proteins, essential for carrying out replication, maturation, and genome packaging of SARS-CoV-2 [23][24]. The genomic RNA gets translated to produce two overlapping polyproteins, pp1a and pp1ab (formed after -1 ribosomal frameshifting mechanism), that are proteolytically cleaved and processed into 16 nsPs by two virus-encoded cysteine proteases, the PLpro and the Mpro [25][26]. These nsPs form the replication and transcription complex (RTC) responsible for directing the process of transcription, replication, and maturation of the viral genome [23][24][27]. SARS-CoV-2 PLpro, a domain within nsP3 protein, is a cysteine protease that recognizes the P4-P1 consensus LXGG sequence and cleaves the peptide bond between nsP1/nsP2 (LNGG↓AYTR), nsP2/nsP3 (LKGG↓APTK), and nsP3/nsP4 (LKGG↓KIVN) [9][28]. It shares a sequence identity of 83% with PLpro of SARS-CoV and is relatively distant from MERS with a sequence identity of 32.9% [29][30]. As an evasion mechanism against the host innate immune response, PLpro possesses deubiquitination and deISG15ylation activities that cleave off ubiquitin and ISG15 (ubiquitin-

like interferon-stimulated gene 15) post-translational modifications from host proteins by recognizing the C-terminal RLRGG sequence [30][31][32]. SARS-CoV-2 PLpro exhibits a differential preference for host substrate, cleaving ISG15 more preferentially, whereas PLpro of SARS-CoV predominantly cleaves off ubiquitin chains [25][30]. Interestingly, the multifunctional PLpro inactivates TBK1, a kinase required to activate transcription factor interferon responsive factor 3 (IRF3), prevents dimerization and translocation of IRF3 to the nucleus, and blocks NF-κB signaling pathway, eventually attenuating the type I interferon response of the host cell [25][31][33]. Due to the dual role of PLpro in replication and pathogenesis of SARS-CoV-2, targeting PLpro may have an advantage in not only suppressing viral infection but also in restoring the dysregulated signaling cascades in infected cells that may otherwise lead to cell death in the surrounding, non-infected cells. Despite extensive efforts in drug designing and lead optimization, the development of PLpro inhibitors is challenging and still remain at the preclinical stage with only a few covalent and non-covalent inhibitors reported till date [34], [35], [36] .

Of note, PLpro has a right-handed "thumb-palm-finger" architecture which is similar to that of host deubiquitinating enzymes (DUBs), the ubiquitin-specific protease (USP), despite very low sequence similarity between them (~10%) [25]. SARS-CoV-2 PLpro has two domains, the "thumb-palm-finger" catalytic domain at the C-terminus and a small N-terminal ubiquitin-like (UBL) domain [25][33][37]. The active site of PLpro is made up of a canonical cysteine protease triad of Cys111, His272, and Asp286 residues, located at the interface of thumb and palm sub-domains. The most complex architecture is of the fingers subdomain, as it is made up of two α-helices, six β-strands, and a zinc-binding loop that is indispensable for maintaining structural integrity [25][38]. An important flexible β-turn/loop, blocking/binding loop 2 (BL2 loop) that recognizes the P2-P4 of the LXGG motif of the substrate and closes upon binding of substrate/inhibitor, is located between β11–12 strands spanning the residues from 267–271, [30][38].

PLpro shares a strikingly similar USP fold like the cellular DUBs, with a structurally conserved active site fold and orientation of catalytic triad residues Cys-His-Asp/Asn. Previous studies have reported successful identification and repurposing of USP inhibitors against SARS-CoV and MERS [39][40][41]. These drugs effectively inhibited SARS-CoV after interacting with the residues of the substrate binding sites [40]. Therefore, repurposing USP inhibitors is an attractive alternative strategy that can assist in quickly identifying potentially effective molecules against SARS-CoV-2 PLpro due to the structurally conserved active site fold. Moreover, inhibitors with a cyanopyrrolidine warhead, such as gliptins, are reported to initiate a β-elimination reaction in the active site of USPs, resulting in irreversible inactivation of active site cysteine to dehydroalanine after desulfhydration reactions [42][43]. These gliptins are already in clinical use as an antidiabetic compound inhibiting dipeptidyl peptidase 4 (DPP4), a serine protease and a possible receptor for SARS-CoV-2 entry [43][44][45]. Notably, the DPP4 inhibitor, sitagliptin, is reported to exert an anti-inflammatory effect on the lungs by inhibiting the IL-1 and

IL-6 inflammatory pathways, eventually providing some relief against acute respiratory distress syndrome (ARDS) [46][47][48]. Repurposing gliptins and DUB inhibitors are hypothesized to serve a dual mode of action in inhibiting SARS-CoV-2; firstly, by the possible inhibition of enzymatic activity of PLpro and secondly, via restoration of host innate immune responses [49].

The present study aims to repurpose and identify currently available DUB inhibitors and cyanopyrrolidine ring containing compounds against PLpro of SARS-CoV-2 by exploiting the catalytic site and S2-binding pocket of PLpro. High-throughput virtual screening, docking, and simulation experiments identified five compounds with docking scores comparable to known PLpro inhibitor, GRL0617, suggesting their potentiality as SARS-CoV-2 inhibitors. The compounds were assessed for their inhibition of SARS-CoV-2 PLpro and anti-coronaviral activity. Two of these compounds, Lithocholic acid and Linagliptin exhibited significant binding affinity, and greater inhibitory potency against PLpro enzyme and SARS-CoV-2 replication across multiple cell lines. Next, to dissect the mechanism of action of identified inhibitors, the crystal structure of Linagliptin and Lithocholic acid in complex with PLpro was also determined in this study that uncovered new binding sites and provided a structural basis for their inhibitory mechanisms. Further, the compound, Linagliptin, was selected as an optimized lead and it's anti-SARS-CoV-2 activity was characterized *in vivo* using a mouse-adapted SARS-CoV-2 model. Overall, the X-ray crystal structures and activity profiling studies presented herein opens a new avenue of repurposing DUB inhibitors against PLpro of SARS-CoV-2 and recommends the compound Linagliptin as a promising therapeutic candidate.

MATERIAL AND METHODOLOGY

1. Cells, viruses, and compounds

Vero and HEK293T cell line used in this study were procured from NCCS (Pune, India). The cells were maintained in high glucose Dulbecco's-modified essential media (DMEM; HiMedia, India) augmented with 10% heat inactivated fetal bovine serum (FBS; Gibco, USA), 100 units of penicillin, and 100 mg streptomycin/mL. HEK293T cells expressing human ACE2 (HEK293T-ACE2) (NR-52511, BEI Resources, NIAID, NIH) and A549 cells (NCCS, Pune, India) transduced to stably express human ACE2 receptor (A549 ACE2), were used for SARS-CoV-2 infection. HEK293T-ACE2, HEK-293T, and A549-ACE2 cells were cultured in complete media prepared using DMEM (12100-038, Gibco) supplemented with 10% HI-FBS (16140-071, Gibco), 100 U/mL Penicillin-Streptomycin (15140122, Gibco) and GlutaMAX™ (35050-061, Gibco). Assessment of cytotoxic effect and the inhibitory potential of identified compounds against SARS-CoV-2 replication was carried out in Vero cells, HEK293T-ACE2, and A549-ACE2. HEK-293T cells (NCCS, Pune) were used for pro-inflammatory cytokine quantification assay and interferon (IFN) induction assay.

The wild type SARSCoV-2/Human/IND/CAD1339/2020 strain was isolated from laboratory confirmed COVID-19 patients in India. After genetic characterization by whole

genome sequencing (GenBank accession no: MZ203529), the virus was passaged in Vero cells and supernatant was collected and clarified by centrifugation before being aliquoted for storage at −80 °C [50]. Virus titer was measured in Vero cells by $TCID_{50}$ assay. SARS-CoV-2 isolate Hong Kong/VM20001061/2020 (BEI resources NR-52282), 2020 (hereby referred as SARS-CoV-2) was propagated and titrated in VeroE6 cells. Teneligliptin, Linagliptin, Lithocholic Acid, Vildagliptin, and Flupenthixol (Cayman, India) were dissolved in DMSO and the stock solutions were prepared. The working concentration of drugs prepared in cell culture media was centrifuged at 10,000 rpm for 10 min, and the supernatant was used for all the assays. All procedures related to SARSCoV-2/Human/IND/CAD1339/2020 virus culture and antiviral studies were handled in Biosafety level 3 facility at Indian Veterinary Research Institute (IVRI), Izatnagar, Bareilly, following standard WHO guidelines. Experiments with SARS-CoV-2 isolate Hong Kong/VM20001061/2020 were performed at the viral biosafety level-3 facility, Indian Institute of Science, Bengaluru, India [51].

2. Plasmid constructs

DNA sequence encoding the PLpro of SARS-CoV-2 was codon optimized for bacterial expression [52]. PCR amplification of the gene encoding PLpro was carried out using synthesized gene (Invitrogen, Thermo Fisher scientific) as the template. After restriction digestion, the gene was cloned into the Nde1 and Xho1 restriction sites of pET28c bacterial expression vector using 5'-CAGCCATATGGAAGTTCGTACCATTAAAGT TTTTAC-3' forward primer and 5'-GGTGCTCGAGCTATTTGATGGTGGTG-3' reverse primer. The resulting plasmid was transformed into competent DH5α cells. These transformed cells were grown on Luria–Bertani (LB) agar plates supplemented with 50 µg/mL kanamycin with incubation at 37 °C overnight. Several colonies were picked and grown in 10 mL LB broth containing 50 µg/mL of kanamycin. Using the wild type PLpro plasmid as the template, site directed mutagenesis was performed to generate an active site mutant (C111S) by an overlapping PCR strategy, using 5'-AAATGGGCAGATAATAACTCGTATCTGGCAACCG-3' forward primer and 5'-AGTGCGGTTGCCAGATACGAGTTATTATCT-3' as reverse primer. For mammalian expression, gene encoding PLpro was cloned into pcDNA3 vector between BamH1 and Xho1 restriction sites using forward primer 5'-ATGAGGATCCATGGAAGTTCGTACCATTAAAGTTTTTACCA-3' and reverse primer 5'-GGTGCTCGAGCTATTTGATGGTGGTG-3' reverse primer. All the clones were verified by DNA sequencing. The plasmids IFN-Beta_pGL3 (Addgene #102597); pRLTK; RIGI 2CARD; plx 304 empty vector (kind gift from Adolfo García-Sastre, Icahn School of Medicine at Mount Sinai, New York) were used for interferon induction experiment.

3. Structural comparison of PLpro and USP protein

Pairwise comparisons of secondary structure elements were performed with the web-based Secondary Structure Matching program (SSM), available within the Protein Data Bank (PDBeFold) [53]. For assessing structural similarities, crystal structures of SARS-CoV-2 PLpro

(PDB ID: 6W9C), HAUSP/USP7 (PDB ID: 2F1Z), and USP2 (PDB ID: 5XU8) were downloaded from RCSB-PDB [54]. The structures were fed into the PDBeFold-SSM portal and the hits from each pairwise comparison are ranked by their RMSD values, Q-score, and the number of aligned residues. The 3D alignment file was downloaded and analyzed in PyMOL [55] to observe conserved loops and residues. To gain more insights into the conserved residues at the substrate binding pockets (Ub/ISG15 binding site), multiple sequence alignment of SARS-CoV-2 PLpro (PDB ID: 6W9C), HAUSP/USP7 (PDB ID: 2F1Z), and USP2 (PDB ID: 5XU8) was done using Clustal Omega/ESPript 3.0 [56].

4. Structure-based identification of inhibitors

An *in-house* library of ~81 compounds containing previously reported DUBs inhibitors and cyanopyrrolidine ring compounds was prepared, and screened against PLpro to identify potential antivirals against SARS-CoV-2 (supplementary table 1). The SDF files for three-dimensional structures (3D) of all compounds were retrieved from PubChem (https://pubchem.ncbi.nlm.nih.gov/) database. 3D-crystal structure of PLpro of SARS-COV-2 (PDB ID: 6W9C) was retrieved from RCSB-PDB. Using the automated function of AutoDock Vina [57], refinement of protein was done by addition of polar hydrogen atoms and the protein was saved in PDBQT format for further docking studies.

Before performing structure-based virtual screening, all the ligands were energy minimized by Universal Force Field (UFF) using Open Babel in PyRx 0.8 [58], [59]. SDF files of all ligands were converted into PDBQT format for virtual screening against PLpro using an in-built Open Babel and AutoDock Vina module of PyRx 0.8. The grid centers for docking search space were set as X= -34.15, Y= 20.39, and Z=33.83, and the dimensions (Å) for X, Y, and Z axis were set as 36.46, 27.89, and 31.02 respectively. The size of the grid box was set centering on the substrate binding site for PLpro with a default exhaustiveness value of 8 for all ligands. A total of 9 different poses were generated for each ligand. Visual examination of the docked complexes possessing the highest binding affinities was carried out using PyMOL for analyzing hydrogen and hydrophobic interactions. The top-ranked compounds possessing highest binding affinities and displaying key interactions with the targeted site were selected.

Molecular docking of the top-hit ligands with PLpro of SARS-CoV-2 was carried out was carried out at two target sites, the substrate binding cleft and the S2-binding site, using AutoDock 4.2.6 [57]. Crystal structure of PLpro of SARS-CoV-2 (PDB ID: 6W9C) was downloaded from PDB and the PDBQT file of this energy minimized structure was used. AutoDock and AutoGrid tools available with AutoDock4 were used to calculate grid maps for pre-calculation of interaction energies of all interacting atoms. The center points for substrate-binding cleft were set as X= -34.430, Y= 27.180, and Z= 33.900; grid box dimensions were 100 Å ×100 Å×100 Å. Grid box dimensions for re-docking studies at the S2-binding sites were 80 Å ×60 Å×80 Å and grid center points were set as X= -17.693, Y=40.944, and Z= 11.585. Lamarckian genetic algorithm (GA) with a combination of maximum grid-based energy evaluation method was used for docking studies. The program was run for a maximum number of 25 genetic algorithm runs.

All other parameters were set as default. Commonly known PLpro inhibitor GRL0617 was used as a reference control. Out of all the possible poses generated, the pose showing maximum binding affinity, hydrogen, hydrophobic interactions, and lowest RMSD values were chosen for detailed visual analysis using LigPlot and PyMol. Top 20 ligands displaying interactions similar to GRL0617 for targeted site of PLpro, possessing high binding affinities, and low RMSD values (< 2 Å) were sorted out. Of these hits, the compounds that were recently reported as SARS-CoV-2 inhibitors in other studies were excluded from further studies.

To gain a deeper understanding of the stability of protein-ligand docked complexes, MD simulation was carried out for the docked complexes of ligands targeting the substrate binding cleft and the S2-binding site, using GROMACS 2022.2 program with a CHARMM force field on Ubuntu-based LINUX workstation. For performing all MD simulations of protein-ligands, the topology files of selected ligands were generated using CHARMM36 General Force Field (CGenFF). The protein-ligand complexes were solvated in a cubic box and the steepest descent algorithm for 50,000 iteration steps was used to perform energy minimization. Two different system equilibration phases were carried out for 500,000 steps. The first phase of system equilibration was performed at a constant number of particles, volume, and temperature (NVT) at 300K with short range electrostatic cut-off of 1.2 nm. The second phase involved a constant number of particles, pressure, and temperature (NPT) ensemble at 300 K, for each step of 2fs. Finally, the MD simulation was carried out for 100 ns with integration time frame steps of 2 fs. The Root Mean Square Deviation (RMSD) values were calculated for PLpro protein and for all protein-ligand complexes.

5. PLpro expression, purification, and inhibition assay

For expression in *E. coli*, the plasmid coding for PLpro was transformed into expression host *Rosetta* (DE3; Novagen, USA) and the culture in LB broth medium at 37 °C. The expression of PLpro protein was induced using 0.5 mM isopropyl-β-d-1-thiogalactopyranoside (IPTG) along with the addition of 1mM $ZnCl_2$ to log phase culture (OD_{600} = 0.6), and the cells were further grown overnight at 18 °C and 180 rpm in an incubator. Cells were harvested by centrifugation (6000 rpm for 10 min at 4 °C) and were resuspended in lysis buffer (50 mM Tris-HCl, pH 8.5, 500 mM NaCl, and 5mM DTT). Cells were homogenized using French press (Constant Systems Ltd, Daventry, England) and the cellular debris was removed by centrifugation at 10000 rpm for 1.5 h at 4 °C. The clarified supernatant was loaded onto pre-equilibrated nickel-nitrilotriacetic acid (Ni-NTA) (Qiagen, USA) affinity column and flow-through was collected after incubation for 30 min at 4 °C. After washing the resin with binding buffer (50 mM Tris-HCl, pH 8.5, 500 mM NaCl, and 5mM DTT), the recombinant histidine tagged PLpro protein was eluted with 100-500 mM imidazole in binding buffer. The eluted fractions were analyzed using 15% sodium dodecyl sulphate-polyacrylamide gel electrophoresis (SDS-PAGE). The fractions containing pure PLpro protein were pooled together and dialyzed against buffer containing 20 mM Tris-HCl, pH 8.5, 200 mM NaCl, and 5mM DTT. The dialyzed protein was concentrated using Amicon centrifugal filters (Millipore, Burlington, MA, USA) with a molecular weight cutoff of

10 kDa. The concentration of purified PLpro was determined by using the Bradford Assay. Expression and purification of C111S mutant was performed using the same protocol as that for the wild type PLpro.

To characterize *in vitro* enzymatic activity of SARS-CoV-2 PLpro and to assess the inhibitory potential of identified compounds, a high-throughput fluorescence resonance energy transfer (FRET) based enzymatic assay was developed as described previously [9]. To carry this out, a commercially available fluorogenic substrate Z-Arg-Leu-Arg-Gly-Gly-7-amido-4-methylcoumarin (Z-RLRGG-AMC) (Biolinkk, India) representing the C-terminal residues of ubiquitin was used. The experiment was carried out in 96-well non-binding black plates (Corning) in reaction buffer containing 50 mM HEPES (pH 7.5). The protease diluted in reaction buffer was added to each well at a final concentration of 1 μM. Enzymatic reaction was initiated with the addition of fluorogenic substrate peptide at a concentration of 1.5 μM and the fluorescence signals were monitored continuously using a plate reader (Synergy HT, BioTek Instruments, Inc) with filters for excitation at 360/40 nm and emission at 460/40 nm for 30 min. PLproC111S was used as a negative control to determine whether signal generation was dependent on proteolytic activity of enzyme. Data from duplicate set of readings was averaged together to plot a graph for relative fluorescence and time.

To assess the inhibitory potential of screened compounds, the assay was assembled as follows: 1 μM PLpro in 50 mM HEPES buffer was incubated with increased concentration of compounds (Cayman chemicals, USA) ranging from 0.1 μM to 500 μM and was dispensed into wells of 96-well plate. Reactions were initiated with 1.5 μM of fluorogenic substrate peptide and the fluorescence signals were monitored continuously for 10 min at excitation wavelength of 360/40 nm and emission wavelength of 460/40 nm. Data from duplicate set of readings were averaged together and a graph for percentage inhibition vs concentration was plotted for each selected compound after non-linear curve fitting using GraphPad Prism. Concentration of inhibitor that resulted in 50% inhibition (IC_{50}) was calculated.

6. Binding kinetic analysis using Surface Plasmon Resonance (SPR)

The binding kinetics and affinity of identified compounds to PLpro of SARS-CoV-2 were analyzed by SPR using a Biacore T200 system (GE Healthcare) at 25 ˚C. In brief, histidine-tagged PLpro was diluted to 10 μM concentration at pH 7.3 and was then captured on NTA chip in 1X Phosphate buffer saline (1X PBS) running buffer (137 mM NaCl, 2.7 mM KCl, 10 mM Na_2HPO_4, and 1.8 mM KH_2PO_4) degassed and filtered through 0.22 μM membrane filter. The binding kinetic studies were performed by collecting the data at 25°C by injecting the concentration series of analyte over the surface of chip having the immobilized PLpro with the following injection parameters: 10μL/min flow rate and 60 s association and dissociation phases. The surface was regenerated after each dissociation phase. Equilibrium dissociation constants (K_D) of each pair of PLpro-ligand interaction were calculated using Biacore Evaluation Software (GE Healthcare) by fitting to a 1:1 Langmuir binding model.

7. Cytotoxicity and viral load reduction assay

To determine the cytotoxic profiles of identified compounds on Vero cells, HEK293T-ACE2, and A549-ACE2, MTT assay was performed as described previously [60]. Briefly, cells were seeded onto wells of 96-well cell-culture plate at a density of 1×10^4 cells/well and the plates were incubated at 37 °C and 5% CO_2 overnight for proper adherence of cells. The culture media was removed and the monolayer of cells was treated with increased dilutions of compounds (1-100 μM) prepared in DMEM media in triplicates. Post incubation period of 48 h, the media was removed, MTT [3-(4,5-dimethylthiazol-2-yl)-2,5-diphenyl tetrazolium bromide] solution (5 mg/mL) was added and incubated for 4 h at 37 °C in a humidified incubator with 5% CO_2. Following this, the MTT solution was removed and the formazan crystals were dissolved in DMSO. Absorbance was measured at a wavelength of 550 nm using a multimode plate reader (Synergy HT, BioTek Instruments, Inc). Results were expressed as percentage viability of cells in comparison to untreated cell control. Percentage viability for each compound was calculated and a dose-response curve was plotted using GraphPad Prism software.

Viral load reduction assay was performed by quantitative reverse transcription-polymerase chain reaction (qRT-PCR). Briefly, Vero cells were seeded and cultured in 24-well plate in DMEM media supplemented with 10% FBS and 100 units of penicillin and 100 mg streptomycin/mL, at 37 °C and 5% CO_2. Three hours before infection, the cells were washed with PBS and the media was replaced with DMEM (2% FBS) containing gradient of diluted experimental compounds. Post incubation, the cells were washed with PBS and were infected with SARS-CoV-2 at a Multiplicity of infection (MOI) of 0.01 in media without FBS and again incubated for 1.5 h. After incubation, the viral inoculum was removed and the cells were washed with PBS and then replenished with fresh medium containing dilutions of compounds. Plates were then incubated for 48 h at 37 °C and 5% CO_2. At 48 hours post infection (hpi) the plates were freezed at -80ºC. On the following day plate was thawed, and viral RNA was extracted from cell lysate of SARS-CoV-2 infected cells using HiPurA™ Viral RNA Purification Kit, according to the manufacturer's instructions. One-step qRT-PCR was performed with primers targeting the SARS-CoV-2 envelope (E-gene) and RdRP region using the commercially available COVISure-COVID-19 Real-Time PCR kit (Genetix), as per the manufacturer's instructions, to quantify the virus yield. The thermocycling conditions consist of 15 min at 50 °C for reverse transcription, 95 °C for 2 min, followed by 40 cycles of 30 s at 95 °C and 30 s at 60 °C. All experiments were performed in duplicates. Percentage inhibition was calculated based on ΔΔCt. The percentage inhibition versus concentration graph was plotted to calculate the EC_{50} values using the linear regression.

Infectious virus production by compound treated and infected cells as compared to only infected cells was also evaluated by the standard 50% tissue culture infectious dose ($TCID_{50}$) and was expressed as $TCID_{50}$/mL [61]. For this purpose, 4×10^4 Vero cells/well were seeded in a 96-well plate and the plate was incubated at 37 °C and 5 % CO_2, till confluency. The freeze-thawed cell lysate of cells infected and treated with different concentrations of compounds collected at 48 hpi of the antiviral assay was subjected to 10-fold serial dilutions (10^1 to 10^8). Compound

untreated and infected samples were used as positive control, and samples with only cell-culture media were used as a negative control. These dilutions were inoculated on Vero cells. Cells were incubated for 3 to 4 days at 37 °C and 5 % CO_2 [61]. The plate was monitored daily for the appearance of a cytopathic effect (CPE). Post incubation, the viral inoculum was removed, and 10% formaldehyde (in PBS) was used to fix cells for 2 h at room temperature, followed by staining with 0.5% crystal violet solution for 1 h. Percent infected dilutions immediately above and immediately below 50% were determined. $TCID_{50}$ was calculated on the basis of Reed and Muench method [61].

8. Validation of antiviral activity in human cell lines

HEK293T-ACE2 and A549-ACE2 cells were seeded in 24 well plates and used for antiviral assay the next day. Single non-toxic concentrations of Teneligliptin, Linagliptin, Lithocholic Acid or Flupenthixol were prepared in infection medium (DMEM containing 2% FBS) and used to pre-treat cells for 3 h. For Linagliptin and Lithocholic acid, cells were treated with increasing doses of the drugs to estimate IC_{50}. Cells were then washed with warm PBS and infected with 0.01 MOI SARS-CoV-2 in DMEM without FBS for 2 h. The inoculum was then removed, cells washed with PBS and incubated with infection media containing the drug concentrations. After 48 (HEK293T ACE2) or 72 h (A549 ACE2) total RNA was extracted using TRIzol (Thermo Fisher, 15596018) as per manufacturer's instructions, and viral copy number was estimated by qRT PCR.

qRT-PCR: Equal amount of RNA was used to determine viral load using the AgPath-ID™ One-Step RT-PCR kit (Applied Biosystems, AM1005). The following primers and probes targeting the SARS-CoV-2 N-1 gene were used for amplification. Forward primer: 5'GACCCCAAAATCAGCGAAAT3' and Reverse primer: 5' TCTGGTTACTGCCAGTTGAATCTG3', Probe: (6-FAM / BHQ-1) ACCCCGCATTACGTTTGGTGGACC). The Ct values were used to determine viral copy numbers by generating a standard curve using the SARS-CoV-2 genomic RNA standard. All statistical analyses were performed using GraphPad Prism 8.4.3 (GraphPad Software, USA). In all cases, a p-value < 0.05 is considered significant.

9. Pro-inflammatory cytokine quantification assay

HEK293T cells were seeded in wells of 24-well plate before transfection. The media was removed and the cells were stimulated with 1 µg/mL Polyinosinic:polycytidylic acid (poly I:C; Sigma) using Lipofectamine 2000 (Invitrogen). Post incubation period of 6 h, the media over the cells was removed, fresh OptiMEM (Gibco) containing the compounds was added to cells [62], [63]. 24 h post transfection, total RNA isolation was done using TRIzol (RNAiso; Takara) by following manufacturer’s instruction and was reverse-transcribed into first-strand cDNA using PrimeScript™ 1st strand cDNA Synthesis Kit (Takara Bio) in accordance with manufacturer’s protocol. For determination of effects of compounds on interferon, 500 ng of cloned pcDNA3 vector encoding PLpro protein of SARS-CoV-2 was transfected in HEK293T cells using

Lipofectamine 2000 (Invitrogen) as per the manufacturer's protocol. Cells were stimulated 24 h after plasmid transfection with 1 µg/mL Polyinosinic:polycytidylic acid (poly I:C; Sigma) using Lipofectamine 2000 (Invitrogen). After an incubation of 6 h, fresh OptiMEM media containing the compounds was added to cells. Mock treated cells or cells transfected with 500 ng of empty pcDNA3 vector or were included as controls [62], [63], [64]. RNA was isolated and gene expression analyses for IL6, CXCL10, TNFα, and IFN-β cytokines were performed using KAPA SYBR fast universal qPCR kit (Sigma-Aldrich, USA) on QuantStudio real-time PCR system (Applied Biosystems, IN) with the expression of β-actin as the internal control. Based on the ΔΔCt method, The fold change in infected cells compared to corresponding controls was calculated after normalizing to the β-actin gene. All reactions were carried duplicates in a 96-well plate (Applied Biosystems, IN). Fold change was calculated by taking cells treated with poly(I:C) as 1. The primer sequences used for qRT-PCR are listed in supplementary Table 2.

10. Interferon induction assay

HEK-293T cells were co-transfected with 50 ng IFNβ-luc firefly luciferase reporter plasmid, 20 ng RIGI 2CARD and 20 ng of pRL-TK Renilla luciferase reporter plasmid, along with/not 500 ng of plasmid expressing SARS-CoV-2 PLpro or empty vector. Transfection was done using Lipofectamine™ 2000 Transfection Reagent (11668019, Invitrogen) as per manufacturer's instructions. 3 h post transfection, the media was replaced with complete medium containing 50 µM Teneligliptin, 50 µM Linagliptin, 25 µM Lithocholic Acid or 10 µM Flupenthixol. Cells were incubated for 24 h post transfection, then harvested in passive lysis buffer (E1941, Promega) and luciferase expression quantified using a dual luciferase assay (E1980, Promega). All statistical analyses were performed using GraphPad Prism 8.4.3 (GraphPad Software, USA). In all cases, a p-value < 0.05 is considered significant.

11. Crystallization and structure determination

Purified SARS-CoV-2 PLpro, in the inactive mutant form (C111S), was crystallized using sitting-drop vapor diffusion method. To achieve this, the purified protein was concentrated up to 15 mg/mL and the crystal trays were set up at various protein-to-precipitant ratios (1:1, 2:1, and 1:2) with reservoir buffer containing crystallization condition [0.1 M Tris-HCl (pH 7.5-9.0), 1.4 M NaH_2PO_4, and 2-15% Glycerol] in 96-well sitting-drop plate (Corning, USA). Diffraction quality crystals were produced after 1 week at 4 °C. The crystals were manually harvested from the drop and were cryo-protected by reservoir well solution plus 10% glycerol and snap-frozen in liquid nitrogen for diffraction data collection. For co-crystallization of PLproC111S-Lithocholic acid complex, a10-fold molar excess of the inhibitor was added to PLproC111S (15mg/mL) and was incubated overnight at 4 °C. The sample for complex was then clarified by centrifugation at 10,000 rpm for 20 min followed by setting up of crystal tray using sitting drop vapor diffusion method at protein-to-precipitant ratio of 1:1 using crystallization condition similar to that for native PLpro [0.1 M Tris-HCl (pH 7.5-9.0), 1.4 M NaH_2PO_4, and 2-15%

Glycerol]. To obtain Linagliptin soaked PLpro crystals, apo crystals for PLproC111S were transferred into crystallization solution supplemented with Linagliptin for 1 h at 4 °C and were then cryoprotected in reservoir liquor supplemented with 10% glycerol.

Single-crystal X-ray Diffraction data for PLproC111S apo and its complex with identified compounds was collected at the Home Source, Macromolecular crystallography Unit, IIC, IIT Roorkee. Datasets were processed using Aimless module of CCP4i2 and the structures were determined by molecular replacement (also a part of the CCP4i2 package) with a SARS-CoV-2 PLpro structure (PDB 6WRH) as a search model. Models for SARS-CoV-2 PLproC111S and its complex with selected compounds were subjected to sequential rounds of model building using COOT and refinement of atomic coordinates and B-factors in refmac5 that allowed for the correct placement of sidechains and loops. All structural analysis and figure preparation was carried out by software PyMOL (Schrödinger, New York, NY, USA). Models were validated with MolProbity. The parameters for X-ray data collection and refinement statistics are presented in

12. HPLC:

High-Performance Liquid Chromatography (HPLC) analysis for inhibitor was carried out on a Waters HPLC system equipped with Sunfire C18 reverse-phase column (250 × 4.6 mm, 5 µm particle size), 1525 binary pump and 2998 photodiode array detector (PDA). The degassed and vacuum filtered mobile phase consisted of water containing 0.1% Orthophosphoric acid pH 4.3 (A) and methanol (B) which were employed in the isocratic flow of 9A: 41B at a flow rate of 0.5 mL/min. Injection volume was set 20 µL and the column temperature was 28 °C. The ligand was monitored at 230 nm. Sample peaks were identified by matching retention time and UV spectrum with authentic standards.

Results:

PLpro is a deubiquitinating and deISGylating enzyme

Structural studies have contributed to a detailed understanding of SARS-CoV-2 PLpro with other DUBs. Reminiscent of the overall architecture of DUBs of the USP family, PLpro shares a similar active site architecture with host USP7 (also known as HAUSP) and USP2 proteins, including the signature catalytic triad (Cys-His-Asp/Asn) at the interface of its thumb and palm domains. A detailed structural comparison of the PLpro with UPS7 and USP2 proteins was carried out using the PDBeFold (SSM: Secondary Structure Matching) and multiple sequence alignment was performed with ESPript3 (Supplementary Figure 1). Although these proteins share a very low percentage of sequence identity with an alignment of only 187 residues of PLpro with USP7 and USP2 proteins, the structural superimposition topologies are reasonably similar with an overall RMSD value of 1.68Å and 1.24 Å for USP7 and USP2, respectively (Figure 1). Briefly, the palm subdomain of PLpro, USP7, and USP2 comprises of 6 β-sheets and includes the conserved catalytic triad (Cys-His-Asp/Asn) of the active site. Beyond the catalytic residues,

USPs contain N- and C-terminal extensions that aid in substrate recognition and binding. The BL2 loop of SARS-CoV-2 PLpro (residues 267–272) that provides floor to ubiquitin tail, also superimposes well with the BL2 loops of USP7 and USP2 (Figure 1) [65][66]. Interestingly, the zinc-binding domain located in the thumb region of SARS-CoV-2 comprises of 4 cysteine residues (Cys189, Cys192, Cys224, and Cys226) and the same pattern is observed for USP2 as well (Cys334, Cys337, Cys381, and Cys384) [67]. Contrastingly, some of the four cysteine residues of this metal binding motif have been mutated during evolution in USP7 and other DUBs due to which the zinc binding ability was lost while the fold integrity was still retained [67]. Importantly, few residues of the substrate binding or proteolytic cleft formed near the BL2 loop occupying the S3/S4 pocket are also conserved. For instance, Gly 269, Gly 271, His 272, and Tyr 273 (numbering as per PLpro) are conserved between USP7 and USP2 signifying that the catalytic site and few adjacent residues are conserved (Figure 1 and Supplementary figure 1) [34][38]. Nevertheless, the structural architecture of the active/catalytic site is very similar in PLpro, USP7, and USP2, suggesting that at least some inhibitors may display cross activity among these proteases.

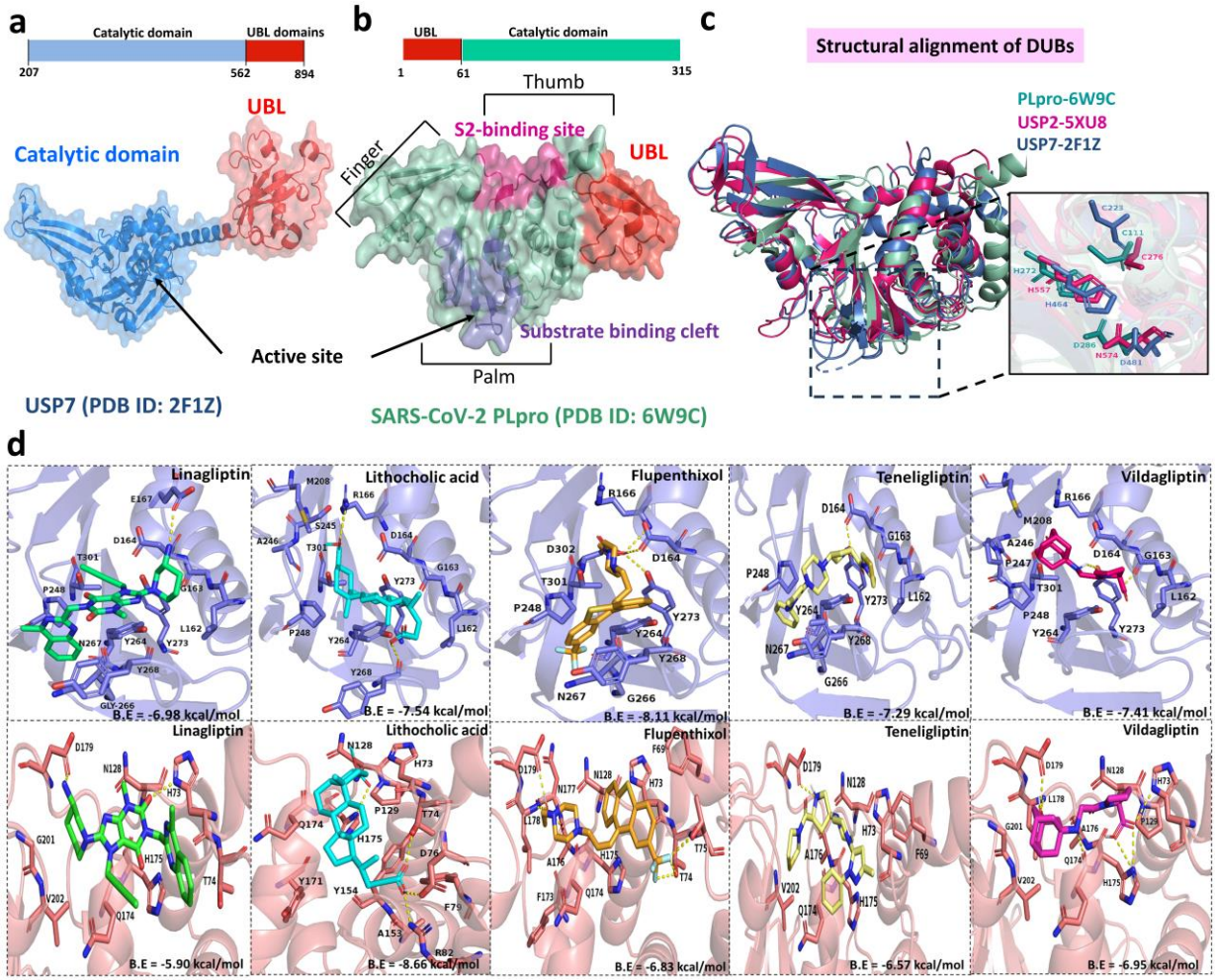

Figure 1: Domain organization and comparison of structural motifs of SARS-CoV-2 PLpro with cellular DUBs USP7. *(a) Surface representation of the domain organization and structural architecture of USP7 (PDB ID: 2F1Z). The catalytic domain is represented in blue and the UBL domain is depicted as red surface. (b) Surface view representation of the overall structure of PLpro (PDB ID: 6W9C) with thumb, palm, and zinc-finger domains marked. The substrate binding cleft is depicted as violet surface, the S2-binding site is represented as pink surface, and the UBL domain is shown as red surface. (c) Structural alignment of secondary structure elements of PLpro (Purple; PDB ID: 6W9C), with the cellular DUBs USP7 (Green; PDB ID: 2F1Z), and USP2 (Magenta; PDB ID: 5XU8). A total of 187 residues of each protein chosen by web-based server PDBeFold, were aligned based on the secondary structure elements. Cartoon representation shows PLpro in green, USP2 in pink, and USP7 in blue. The positioning of catalytic triad residues is represented in magnified view. Catalytic triad residues Cys, His, and Asp of PLpro, USP2, and USP7 represented in sticks, are completely superimposed. (d) PyMOL schematic representations of hydrophobic and hydrogen-bonds of the top-hit screened ligands docked at the substrate-binding cleft (purple) and the S2-binding sites (brick red) of PLpro.*

Structure-based identification of PLpro inhibitors

Crystal structure of PLpro in complex with GRL0617, HE9, and acriflavine inhibitors provides a basis for identifying potential inhibitors targeting the multiple sites on SARS-CoV-2 PLpro [38], [68]. To achieve this, an *in house* library of 81 compounds consisting of previously reported DUB inhibitors and cyanopyrrolidine ring-containing compounds, was subjected to high-throughput virtual screening protocol using an in-built AutoDock Vina module of PyRx 0.8 (Supplementary Table 1). A total of 20 compounds obtained after virtual screening were shortlisted based on binding affinities and RMSD values (<1 Å). The resulting scores of virtual screening for these 20 compounds are listed in Supplementary Table 2. Among these top hits, the compound Pimozide, MF094, FT671, ML323, FT827, GNE6640, and N-cyanopyrrolidine screened and identified in our study, were also reported recently to inhibit proteolytic activity of PLpro of SARS-CoV-2, thereby validating this developed protocol [9][69]. Published literature highlights efficacy of sitagliptin and gemigliptin in type II diabetes mellitus patients infected with SARS-CoV-2 when administered as a monotherapy or in form of a combination therapy [70], [71], [72]. These compounds were therefore omitted from further studies and the remaining compounds were processed to gain further insights into binding modes and stabilities of protein-ligand complexes. Based on binding energies, number of polar/hydrophobic interactions, and availability, a total of five compounds were selected for detailed re-docking and simulation studies followed by *in vitro* investigations.

Binding modes of inhibitors targeting PLpro of SARS-CoV-2

Owing to the structural similarities in active site architecture of PLpro and DUB enzymes, USP2 and USP7, re-docking and simulation studies of selected 5 compounds were carried out using AutoDock4.2.6 and Gromacs. The binding mode of GRL0617 (control molecules) with PLpro revealed an important hot-spot active site covering the residues Leu162, Gly163, Asp164, Glu167, Met208, Pro247, Pro248, Tyr264, Tyr268, Gln269, Gly271, and Tyr273, Thr301 that were targeted in this study for antiviral drug discovery [33][38]. Importantly, PLpro efficiently removes ISG15 (more preferentially) and ubiquitin modifications, dampening inflammation and antiviral signaling. The crystal structures of SARS-CoV-2 PLpro in complex with ISG15 (PDB: 6YVA) clearly demonstrates the binding of N-terminal region of ISG15 to a distal S2-binding site located on PLpro thumb domain, contributing to substrate recognition and differential cleavage (Figure 3.1b, depicted in pink surface) [64], [68]. The C-terminal domain of ISG15 sits on the palm subdomain of SARS-CoV-2 PLpro allowing the C-terminal tail to reach the catalytic site. Key interacting amino acids mediating contacts of N-terminal ISG15 with S2 binding site of PLpro spans between 61-74, including Val66, Phe69, Glu70, and Thr75 (Figure 3.1b, pink surface) [37]. Other contacts of S2Ub or N-terminal ISG15 includes SARS-CoV-2 PLpro residues Asn128, Asn177, and Asp180 from the palm domain (Figure 3.12a) [73]. The core S1-binding residues of PLpro mediating interactions with S1Ub or C-terminal ISG15 includes Asn156, Ser170, Tyr171, Gln174, Thr225, and Lys232 [35], [37]. In conclusion, targeting the

substrate-binding cleft, S1, and the S2 binding sites of PLpro represents a new approach for preventing viral replication and its interaction with host cellular pathways.

The predicted AutoDock binding affinities for the screened top-hit compounds for the active site were in the range of -6.9 kcal/mol to -8.1 kcal/mol (Table 1). While the docking score for the control ligand GRL0617 is − 6.94 kcal/mol. Docking studies of flupenthixol revealed that the compound displays a high binding affinity of -8.11 kcal/mol and forms four hydrogen-bonds with active site residues Asp164, Arg166, Tyr273, and Asp302 (Figure 1D and supplementary figure 2). In addition, hydrophobic interactions between flupenthixol and PLpro complex (Pro248, Tyr264, Gly266, Asn267, Tyr268, Thr301) also contributed to stabilization of this protein-ligand complex (Figure 1D). Lithocholic acid is the second-best candidate that interacts with three H-bonds with targeted amino acids Arg166 and Tyr268 along with ten hydrophobic interactions (Figure 1D and Table 1). Like other top hits, teneligliptin and linagliptin also occupied catalytic groove of PLpro forming H-bonds with key GRL0617 binding residues (Asp164: Teneligliptin; Glu167: Linagliptin) (Figure 1D and supplementary figure 2). The complexes of Teneligliptin and Linagliptin are further stabilized by extensive hydrophobic interactions primarily involving Leu162, Gly163, Pro248, Tyr264, Gly266, Asn267, and Tyr268 substrate binding residues of PLpro (Figure 1d and supplementary figure 2). Similarly, vildagliptin also displayed a network of two H-bonds and ten hydrophobic interactions with the targeted site (Figure 1D, supplementary figure 2, and Table 1).

Due to the important role of S2 binding site of PLpro, redocking studies were also conducted at this site and the data revealed binding affinities in the range of -5.9 to -8.6 kcal/mol. The compound Lithocholic acid, displayed highest binding energy when docked at S2 site, interacted primarily with His73, Thr74, and Phe79, the key substrate interacting residues of S2 site. Likewise, the compound Linagliptin interacted with His73 and Asp179 through H-bond interactions along with additional stabilizing hydrophobic interactions with key S2 site residues. The compound Flupenthixol sustained seven H-bond interactions and other additional hydrophobic interactions with key interacting residues of S2 binding site such as, Phe69, His73, Asn128, Asn177. PLpro-Teneligliptin involved one H-bond with Asp179 and interacted with S2 site through additional hydrophobic interactions. The compound Vildagliptin was stabilized by six H-bond and additional hydrophobic interactions as shown in Table 1 (Figure 1d, Supplementary Figure 2).

To further assess the stability of docked complexes, molecular dynamic simulation of the selected 5 compounds with PLpro was carried out for 50 ns (Supplementary figure 3). The overall ligand/protein complex showed no major differences in the overall stability as observed for only PLpro, with an average RMSD value in the range of 0.1-0.4 Å for all complexes (Supplementary figure 3). All complexes attained equilibrium after and were stable throughout the run. Collectively, the data indicates that the selected compounds are valid starting points for optimization and development of new inhibitors against SARS-CoV-2.

Table 1: *Promising antivirals for PLpro of SARS-CoV-2 obtained after detailed molecular docking and MD simulation studies. Binding energies, hydrogen, and hydrophobic interactions are tabulated.*

Name of compound	Site	AutoDock Binding energies	Hydrogen bonds		Hydrophobic interactions
			Bonds (lig - protein)	Bond length (Å)	
Flupenthixol	Site1	-8.11	O-OD1 (Asp164)	3.17	Pro248, Tyr264, Gly266, Asn267, Tyr268, and Thr301
			O-N (Arg166)	3.16	
			O-OH (Tyr273)	2.95	
			O-OD2 (Asp302)	2.71	
	Site2	-6.83	F1-OG1 and F2-OG1 (Thr74)	2.69 and 2.6	Phe69, His73, Asn128, Phe173, Gln174, His175, Asn177
			F2-N and F2-OG1 (Thr75)	1.10 and 3.12	
			O-O (Ala176)	2.67	
			O-N (Leu178)	2.98	
			O-OD1(Asp179)	2.75	
Lithocholic acid	Site1	-7.54	O4-NE & O3-NH2 (Arg166)	2.87 and 3.05	Leu162, Gly163, Asp164, Met208, Ser245, Ala246, Pro248, Tyr264, Tyr273, and Thr301
			O2-O (Tyr268)	2.80	
	Site 2	-8.66	O1-OG1(Thr74)	2.81	His73, Phe79, Asn128, Pro129, Ala153, Tyr154, Tyr171, Gln174
			O2-OD2(Asp76)	2.86	
			O2-NH2(Arg82)	2.73	
			O3-ND1 (His175)	2.72	
Vildagliptin	Site1	-7.41	O4-O (Gly163)	2.55	Leu162, Asp164, Arg166, Met208, Ala246, Pro247, Pro248, Tyr264, and Thr301
			N1-OH and O2-OH (Tyr273)	3.19 and 3.09	
	Site 2	-6.95	O3-ND1 (His73)	3.14	Asn128, Pro129, Ala176, Gly201, Val202
			N1-O (Gln174)	2.74	
			O3-ND1 and O4-ND1 (His175)	2.98 and 3.16	
			O1-N (Leu178)	2.84	
			C4-OD1(Asp179)	2.71	
Teneligliptin	Site1	-7.29	N3-OD1 (Asp 164)	2.41	Leu162, Gly163, Pro248, Tyr264, Gly266, Asn267, and Tyr268
			N3-OH (Tyr 273)	2.78	
	Site 2	-6.57	N3-OD1(Asp179)	2.58	Phe69, His73, Asn128, Gln174, His175, Ala176, Val202
Linagliptin	Site1	-6.98	N27-OE1 (Glu167)	3.11	Leu162, Gly163, Asp164, Pro248, Tyr264, Gly266, Asn267, Tyr268, Tyr273, and Thr301

	Site 2	**-5.90**	O19-ND1 (His73)	3.03	Thr74, Asn128, Gln174, His175, Gly201, Val202
			N27-OD1 (Asp179)	2.59	

Compounds inhibits proteolytic activity of SARS-CoV-2 PLpro

Having established the enzymatic assay for proteolytic activity of PLpro, the inhibitory potential of five compounds selected from virtual screening and docking studies was quantified. To achieve this, recombinant SARS-CoV-2 PLpro was expressed in Rosetta DE3 and subsequently purified using affinity chromatography. A single band at ~36kDa in SDS-PAGE signified pure PLpro protein (Figure 2a). Proteolytic activity of recombinantly purified PLpro was assessed by the optimized FRET-based protease assay, using the commercially available Z-RLRGG-AMC fluorogenic substrate representing the C-terminal residues of ubiquitin, as described in methodology section (Figure 2b). Purified PLproC111S mutant was used as a negative control to conclude that the production of fluorescence signal generation was exclusively dependent on proteolytic activity of enzyme (Figure 2a and 2b). The same FRET assay was used to assess and validate the inhibitory potential of the identified compounds, Flupenthixol, Lithocholic acid, Vildagliptin, Teneligliptin, and Linagliptin against the enzymatic activity of PLpro. Among these selected compounds, both Lithocholic acid and Linagliptin robustly inhibited proteolytic activity of PLpro with over 80% inhibition of SARS-CoV-2 PLpro and half-maximal inhibitory concentration (IC_{50}) values of 27.5 ± 2.20 μM and 53.1 ± 0.01 μM, respectively (Figure 2d and 2e). The compounds Flupenthixol and Teneligliptin showed IC_{50} values of 53.5 ± 4.09 μM and 259.2 ± 0.72 μM (Figure 2f and 2g). In contrast to it, vildagliptin was not observed to show any significant inhibition with a maximum inhibitory effect of less than 50 percent only (IC_{50} > 500 μM) (Figure 2c). Owing to its low inhibitory potential, vildagliptin was not selected for SPR-based binding kinetic assays and cell-based studies against SARS-CoV-2. Considering the inhibitory potential of the selected four compounds, these primary hits were subjected to a series of SPR-based assays and cell-based studies.

SPR assay demonstrates binding of lead DUB inhibitors to PLpro

Prioritized lead compounds were tested in SPR assay to examine the binding kinetics and affinity of compounds against purified PLpro. After immobilization of histidine-tagged PLpro on Ni-NTA chip, serial dose of selected compounds was allowed to flow over the chip and the time dependent optical signal was recorded. Consistent with the results of FRET assay, a dose-dependent increase in response was observed for binding of Lithocholic acid, Linagliptin, and Flupenthixol to SARS-CoV-2 PLpro. As represented in Figure 2h, the K_D values determined by SPR measurements for Lithocholic acid-PLpro, Linagliptin-PLpro, and Flupenthixol-PLpro are 79.3 μM, 72.6 μM, and 258.1 μM, respectively. SPR data suggested that Lithocholic acid and Linagliptin bind to PLpro with stronger affinity in comparison Flupenthixol (Figure 2h). While fitting the data for Teneligliptin, the derivatives of the binding response and the dissociation were

nonlinear and attempts to fit the data with 1:1 Langmuir Binding model failed with Teneligliptin (data not shown). Together with results of fluorescence assay, SPR data confirms that these top-hits can be taken up for cell-based *in vitro* studies.

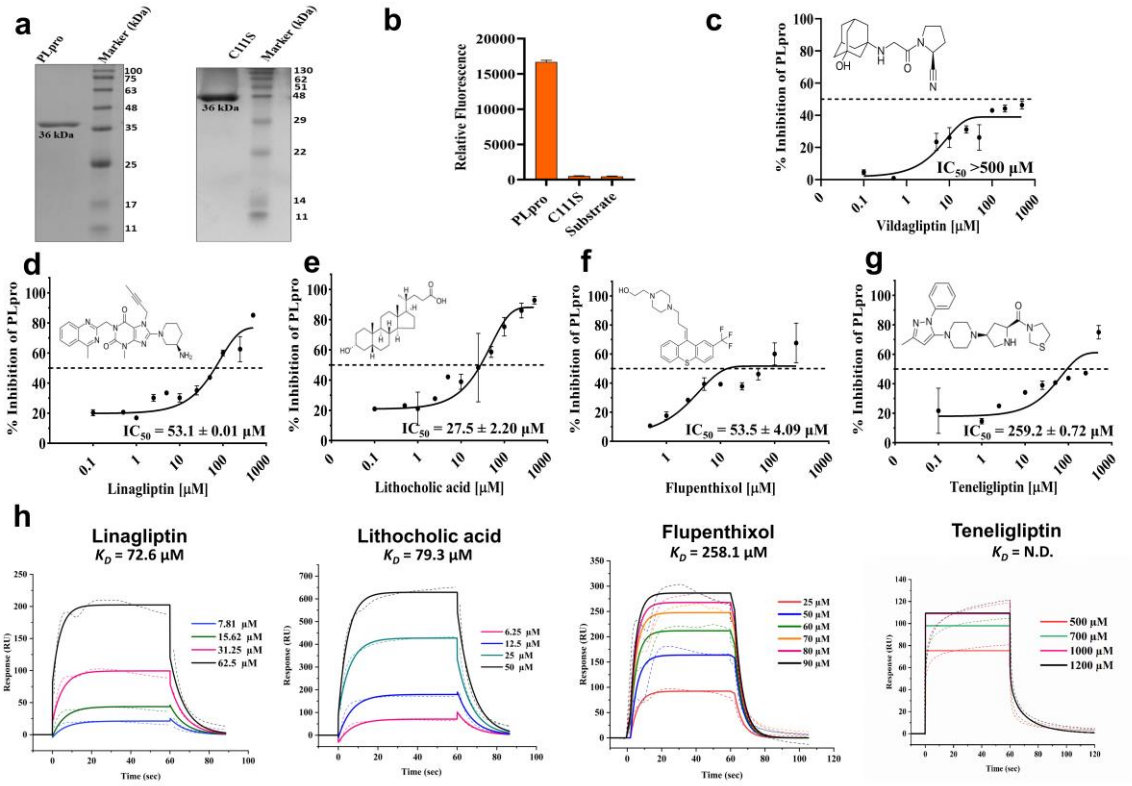

Figure 2: Inhibition of proteolytic activity of PLpro by selected compounds. *(a) SDS-PAGE profile of purified PLpro (~36 kDa) (b)FRET based protease activity comparison of wild type and C111S mutant (inactive) PLpro. Inhibition of proteolytic activity of PLpro by selected compounds. The inhibitory potential of identified compounds (c) Vildagliptin, (d) Linagliptin, (e) Lithocholic acid, (f) Flupenthixol, and (g) Teneligliptin against PLpro were tested using fluorogenic peptide Z-RLRGG-AMC as the substrate. Black dotted lines indicate the concentration of compound needed to inhibit the proteolytic activity of PLpro by half (IC_{50}). All data are shown as mean ± SEM, n = 2 independent experiments (h) Evaluation of binding affinities of Lithocholic acid, Linagliptin, Flupenthixol, and Teneligliptin to SARS-CoV-2 PLpro using SPR. Sensorgrams elucidating the binding kinetics of selected analytes injected successively at increased concentrations against immobilized SARS-CoV-2 PLpro. The data was fitted using 1:1 Langmuir binding model. The processed sensograms are color coded, and the binding response is increasing with the increase in the concentration of the analyte. All experiments were conducted in duplicates. K_D, dissociation constant; RU, response units.*

Inhibitors abrogates replication of SARS-CoV-2 *in vitro*

To ascertain whether the selected compounds were cytotoxic or not, uninfected Vero cells, HEK-293T-ACE2, and A549-ACE2 were incubated with increased concentration of compounds and the cytotoxicity was measured using colorimetric MTT assay. As represented in Supplementary Figure 4, Lithocholic acid, Linagliptin, and Teneligliptin exerted very less cytotoxicity in all cell lines when tested across the range of concentrations (1-100 μM) and their calculated CC_{50} values were more than 100 μM (Supplementary Figure 4). Contrastingly, Flupenthixol displayed slight cytotoxicity at concentrations above 50 μM in the tested cell lines (Supplementary Figure 4). The data suggests safe cytotoxic profile of the selected compounds and qualifies them for evaluation of antiviral potency against SARS-CoV-2.

Based on encouraging inhibitory activity of selected compounds against the PLpro, combined with their low cellular toxicity, we next sought to investigate their *in vitro* efficacy against clinical isolate of SARS-CoV-2 in Vero cells. Cells were pretreated with increased concentrations of compounds (Lithocholic acid, Linagliptin, Teneligliptin and Flupenthixol) and were infected with SARS-CoV-2 at 0.01 MOI, followed by further incubation in medium with compound. Quantification of inhibition in viral replication was done by determining the percentage of positive infected cells in the presence and absence of the compound, at the end of the incubation period. To quantify this, cell lysate of treated and non-treated infected Vero cells was harvested to determine the viral load by quantifying the levels of viral RNA by real-time quantitative PCR (qRT-PCR) targeting the RNA-dependent RNA polymerase (RdRp) and N-protein. Consistent with the results of biophysical studies, Lithocholic acid and Linagliptin effectively inhibited replication of SARS-CoV-2 in Vero cells, exhibiting an EC_{50} value of 21 μM and 14.65 μM, respectively (Figure 3). Surprisingly, Flupenthixol, which was observed to be a relatively weak inhibitor of enzymatic activity of PLpro, also displayed a strong inhibitory effect against SARS-CoV-2 at its non-toxic concentrations with an EC_{50} value of 5.10 μM (Figure 3). Teneligliptin which was relatively a promising inhibitor based on PLpro enzymatic assay also inhibited SARS-CoV-2 infection in Vero cells at low micromolar range (EC_{50} = 20.82 μM) (Figure 3).

To validate the results obtained from qRT-PCR, $TCID_{50}$ based studies were carried out. The effect of compounds on cells infected with SARS-CoV-2 was assessed by performing the virus titration. The sharp decrease in viral titer as compared to non-treated and virus infected positive control was observed in case of Linagliptin (decrease of 4 log $TCID_{50}$/mL) and Teneligliptin (decrease of 2.5 log $TCID_{50}$/mL) (supplementary figure 5). Flupenthixol at the concentration of 20 μM, decreased the viral titer by 1.5 log $TCID_{50}$/mL (supplementary figure 5) and Lithocholic acid (supplementary figure 5) at its highest concentration of 50 μM reduced the titer by 1 log $TCID_{50}$/mL as compared to virus control. We observed that treatment of cells with compounds involved in the present study, significantly reduced infectious virus production and apoptotic cell death associated with virus infection. A concentration-dependent decrease in virus titer was observed in the case of all compounds. Together, the data suggest that these molecules

displayed dose-dependent inhibition of replication of virus in Vero cells and hold considerable promise for therapeutics against SARS-CoV-2.

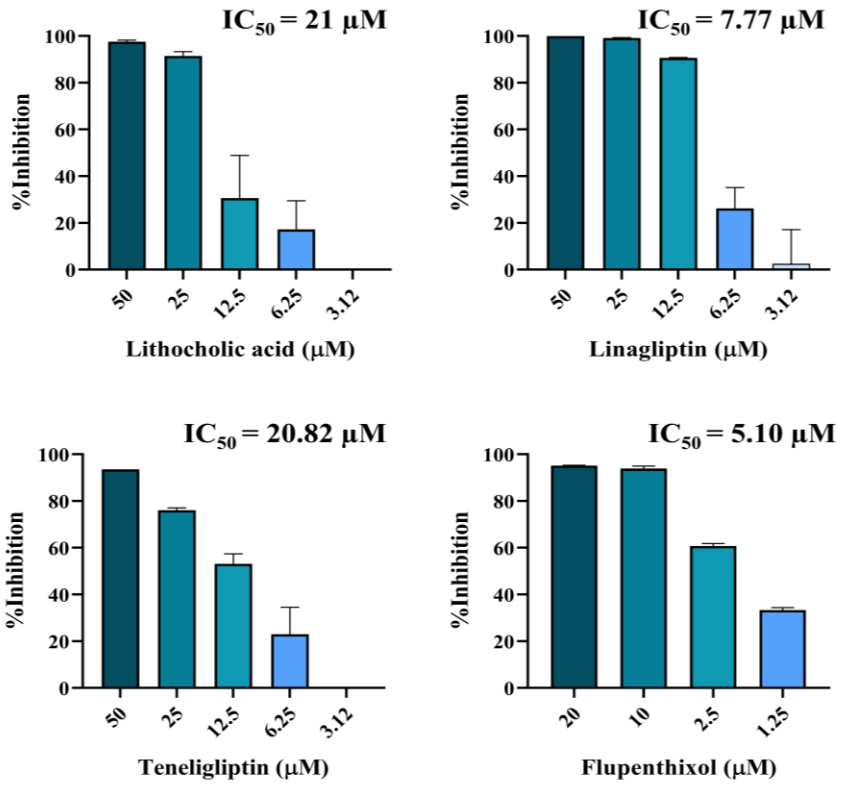

Figure 3: Comparative antiviral efficacy of selected compounds against SARS-CoV-2 infection in vitro. *Vero cells were treated with a series concentration of indicated compounds and were then infected with SARS-CoV-2 at a multiplicity of infection (MOI) of 0.01. Cell culture supernatant was harvested and the inhibition pattern was quantified by qRT-PCR at 48 hpi. Virus inhibition titer (EC_{50}) are estimated from dose–response curves of percentage inhibition versus compound concentration. Representative data are shown from duplicate readings and the final graph was plotted for percentage inhibition of of cells in the presence and absence of compounds (n = 2). Data represent mean ± SD.*

Validation of inhibitory effects in human cell lines

To ensure that the observed antiviral efficacies of identified compounds were not restricted to Vero cells, the compound efficacies were further evaluated on two additional human cell lines expressing ACE2, HEK293T-ACE2 and A549-ACE2 that supports SARS-CoV-2 replication. Cytotoxicity assay was performed in both HEK293T-ACE2 and A549-ACE2 cells to determine the working concentrations of the compounds. Lithocholic acid was toxic in HEK293T ACE2 cells at a concentration of 25 µM, and Flupenthixol at 20 µM concentration led to ~20% loss in cell viability in both cell lines (supplementary figure 4). Based on this, the following highest non-

toxic doses were chosen for the drugs: 50 µM Teneligliptin, 50 µM Linagliptin, 25 µM Lithocholic acid, and 10 µM Flupenthixol.

Antiviral assays were performed using highest non-toxic doses of the four drugs. Dose-titration analysis revealed that nearly all (3 out of 4) tested compounds inhibited replication of SARS-CoV-2 in one or both of these cell lines at potencies equivalent to or greater than those that was observed in case of Vero cells. Results showed consistent inhibition of vRNA loads by a scale of ~ 3 $\log_{10}$, in the presence of 50 µM Linagliptin in HEK293T-ACE2 (IC_{50}= 7.4 µM) and A549-ACE2 (IC_{50}= 0.24 µM) cells respectively (Figure 4a, 4b, 4d, 4e). Lithocholic acid did not show any antiviral effects in HEK293T-ACE2 cells, but inhibited viral load by ~1.5 $\log_{10}$ (IC_{50} = 0.6 µM) in A549 ACE2 cells (Figure 4a, 4c, 4d, 4f). Flupenthixol inhibited viral load by ~ 3 $\log_{10}$ in HEK293T-ACE2 cell line but failed to show any effect in A549-ACE2 cells (Figure 4a and 4d). A possible reason for the differential efficacy of some compounds in different cell lines could be species-specific or cell-type-specific mechanism of action of a given compound or by differences in drug metabolism [73], [74].

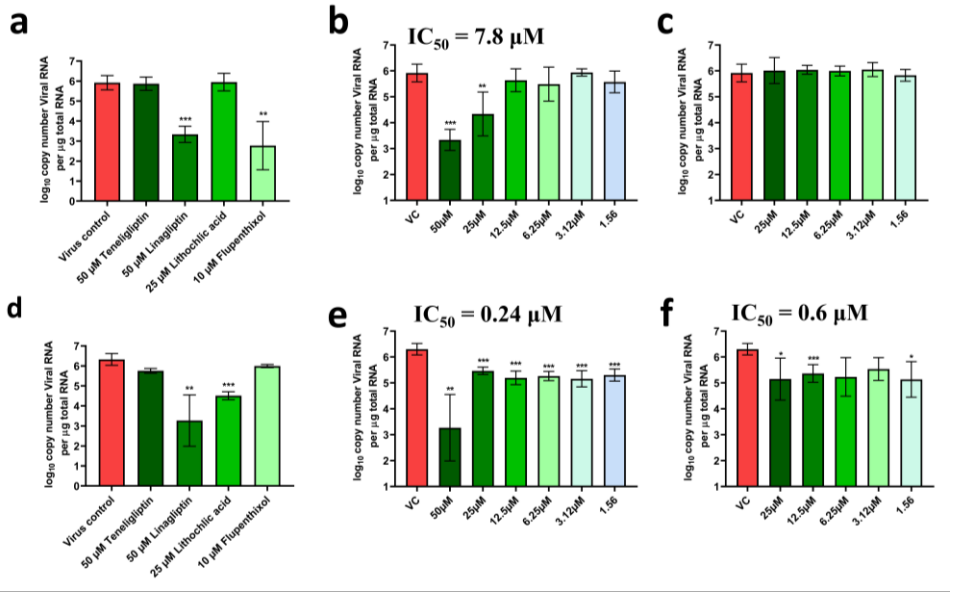

Figure 4: Evaluation of compounds for cellular antiviral potency against SARS-CoV-2 across multiple cell lines. Antiviral assay. *(a-f) Cells were pre-treated with indicated drug concentrations for 3 h, washed and infected with 0.01 MOI SARS-CoV-2 for 2 h in the absence of drugs. After further washing, cells were infected with infection media containing drugs and 48 h later, viral RNA load was estimated from total cellular RNA by qRT PCR. (a) shows results for HEK293T-ACE2 cells treated with single non-toxic concentrations of Teneligliptin, Linagliptin, Lithocholic Acid or Flupenthixol, (b, d) show data for increasing concentrations of Linagliptin and Lithocholic acid respectively. (d-f) represent similar datasets in A549-ACE2 cells. Results represent data from 2 independent experiments. *p < 0.05, **p < 0.01, ***p < 0.001 using Brown-Forsythe and Welch ANOVA with Dunnett's T3 multiple comparison tests. Error bars represent mean ± SD.*

Effects of compound treatment on cytokine expression and IFN responses

Infection by SARS-CoV-2 induces a hyper-inflammatory response driven by the uncontrolled release of TNF-α, IL-6, IL-1, IL-8, CXCL10 or delayed type I interferon response. Therefore, to understand the effects of identified compounds on the expression levels of proinflammatory cytokines induced by SARS-CoV-2, the mRNA expression levels of cytokines were quantified in presence of compounds using qRT-PCR. The data suggests that the compounds Lithocholic acid and Linagliptin were observed to inhibit the expression of IL6 (to a greater extent) and TNFα in HEK293T cells stimulated by Poly I:C, a synthetic analog of dsRNA that mimics virus infection (Figure 5a and b). However, the expression levels of CXCL10 was not affected by the treatment of compounds (Figure 5c). This indicates that treatment with Lithocholic acid or Linagliptin could have an effect on virus induced inflammatory responses (Figure 5a, b, and c). The PLpro of SARS-CoV-2 antagonizes the type-1 IFN innate immune responses of the host cell reducing the amounts of phosphorylated and ISGylated IRF3 or after deubiquitination of stimulator of interferon genes (STING) [75], [76], [77]. Further analysis revealed that the compounds Lithocholic acid and Flupenthixol were able to restore the levels of interferon-beta (IFNβ) in HEK293T cells transfected with SARS-CoV-2-PLpro. By contrast, no effect was observed on the expression levels of IFNβ when cells were treated with Linagliptin and Teneligliptin (Figure 5d and 5e).

To confirm whether the restored levels of IFNβ is due to inhibition of PLpro, a luciferase reporter assay was used to test the effects of drugs on type-1 interferon induction using an IFNβ promoter-driven firefly luciferase reporter plasmid (IFN-Beta_pGL3) and a control plasmid which constitutively expresses renilla luciferase gene (pRL-TK). RIG-I 2CARD was used as an inducer of type-1 IFN induction at a very early step of the signaling pathway upstream of nuclear translocation of IRF3 and expression of interferon stimulated genes (ISGs). The plasmids were co-transfected with plasmid expressing SARS-CoV-2 PLpro to test the effect of the drugs to rescue the viral protein induced inhibition of IFN-beta production. The results of these luciferase reporter assays revealed that PLpro of SARS-CoV-2 suppressed the levels of IFNβ (Figure 5). Having demonstrated a role for expression of SARS-CoV-2 PLpro in attenuating host antiviral IFN pathways, it was anticipated that inhibition by identified compounds would reverse this process. Interestingly, treatment with Lithocholic acid caused ~4-fold increase of IFN-β production signifying that the compound was able to restore the suppressed type 1 interferon responses (Figure 5e and f). Indeed, none of the drugs could rescue the PLpro induced IFN inhibition (Figure 5f). Of all the compounds tested, Linagliptin and Lithocholic acid exhibited significant inhibitory effects across multiple cell lines and were thus selected for further studies.

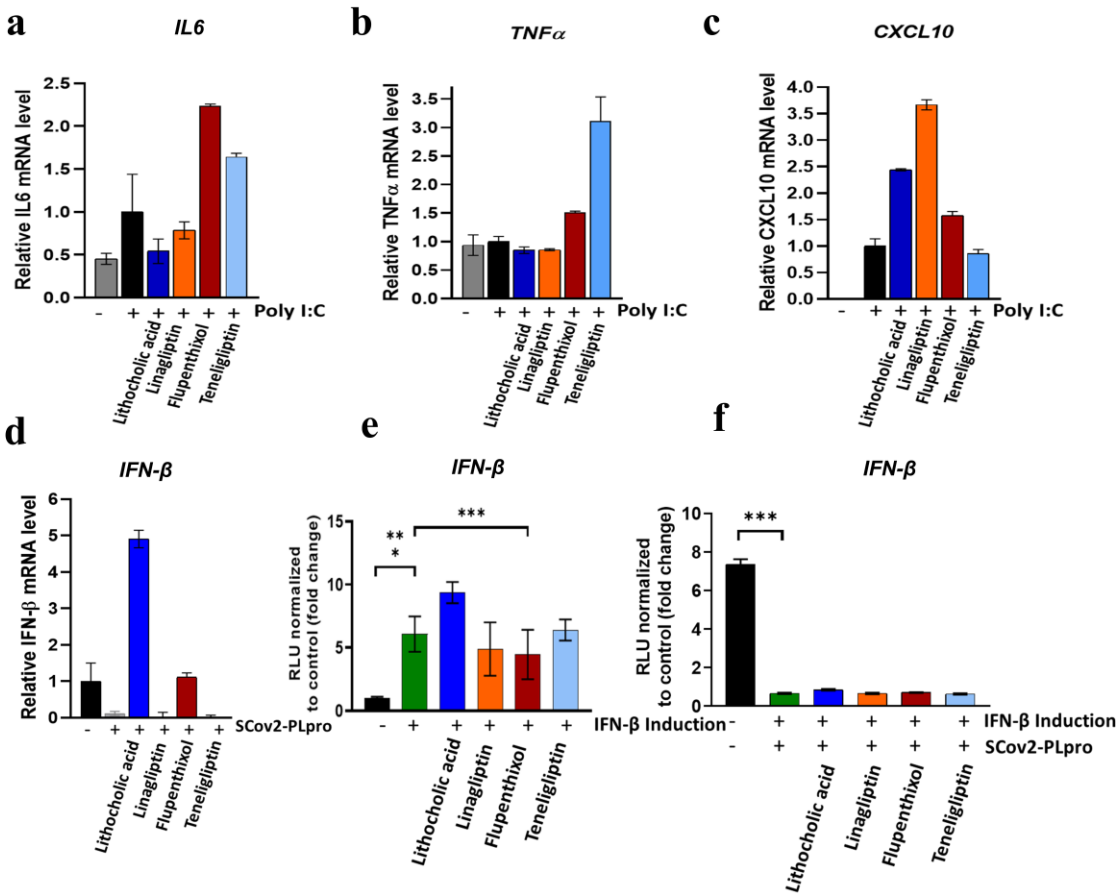

Figure 5. Effects of compound treatment on inflammatory cytokines and delayed type I interferon response. *(a, b, c) HEK293T cells were stimulated with Poly I:C for 6 h and were treated with 30 µM of Lithocholic acid (blue), 30 µM of Linagliptin (orange), 10 µM of Flupenthixol (red), and 30 µM of Teneligliptin (light blue). (d) For evaluation of IFN-β levels, the cells were transfected with plasmid encoding SARS-CoV-2 PLpro followed by stimulation with poly I:C and treatment with compounds. RNA was isolated after 24 h and gene expression analysis for cytokines was performed using qRT-PCR. (e, f) HEK292T cells were transfected with IFNβ-luc firefly luciferase reporter plasmid and pRL-TK Renilla luciferase reporter plasmid, along with plasmid expressing SARS-CoV-2 PLpro or empty vector. RIGI 2CARD was used as an inducer of type-1 interferon production. 3 h post transfection, cells were treated with different drugs 25 µM of Lithocholic acid, 50 µM of Linagliptin, 10 µM of Flupenthixol, and 50 µM of teneligliptin, and 24 h later, cells were collected, and luciferase expression was analyzed by dual luciferase assay. (e) shows results for the effects of drugs on IFN-β promoter activity. (f) shows effects of drugs in rescuing SARS-CoV-2 PLpro induced inhibition of IFN-β production. Results represent data from 2 independent experiments. ***p < 0.001; using One-way ANOVA with Dunnett's T3 multiple comparison tests. Error bars represent mean ± SD.*

X-ray crystal structures of SARS-CoV-2 PLpro in complex with Linagliptin and Lithocholic acid

We next set out to determine crystal structures of PLproC111S in complex with identified inhibitors (Lithocholic acid, Linagliptin, Teneligliptin, and Flupenthixol) to gain comprehensive insights into the molecular mechanisms by which these inhibit the proteolytic activity of PLpro and further SARS-CoV-2 in cell-based conditions. The complex data for PLproC111S:Linagliptin was determined to a resolution of 2.7 Å through crystallization and diffraction at X-ray home source, MCU, IIT Roorkee. Both PLproC111S:Lithocholic acid and PLproC111S:Linagliptin complex belongs to space group P $3_2$21 with one biologically active monomer in the asymmetric unit. Structure factors and atomic coordinates have been deposited with the protein data bank with accession codes PDB ID: 8X1X for PLproC111S: Lithocholic acid and PDB ID: 8XTD for PLproC111S: Linagliptin. Following promising results from *in vitro* studies, we determined a crystal structure of PLproC111S in complex with compounds Linagliptin and Lithocholic acid at a resolution of 2.7 Å and 2.3 Å as a monomer, respectively.

Analysis of the electron density maps signifies that Linagliptin accommodates the ISG15/Ub S2-binding site of PLpro, near the thumb domain, consequently creating sterical hindrance and blocking the N-terminal domain of these substrates from accessing the S2 site (Figure 6). Upon closer examination, Linagliptin was observed to interact with the side chains of surrounding residues, including Phe69, His73, Gln174, Ala176, Leu178, and Asp179 through hydrophobic interactions (Figure 6). The side chains of Asn128, Gln174, and His175 is involved in H-bonding with Linagliptin which occupies the S2-site (Figure 6). Interestingly, Phe69, His73, and Asn128 are critical residues previously shown to interact with ISG15 and Ub substrates [37], [78], [79]. Superimposition of PLproC111S:Linagliptin complex structure with PLpro-ISG15 complex (PDB ID: 6YVA) clearly shows that Linagliptin disrupts the protein-protein interaction between PLpro and ISG15 substrates, thereby prevents the binding of ISG15 to PLpro (Figure 6). Indeed, multiple lost interactions of ISG15 to PLpro also supports the notion of protein-protein interaction (PPI) disruption in presence of Linagliptin. HPLC analysis revealed that Linagliptin displayed a single elution peak at similar retention time points and same UV spectra in control (stock solution) and all reaction conditions (Linagliptin incubated in crystallization buffer at different time points), suggesting that the crystallization buffers have no impact on the structural intactness of the compound (Supplementary Figure 6).

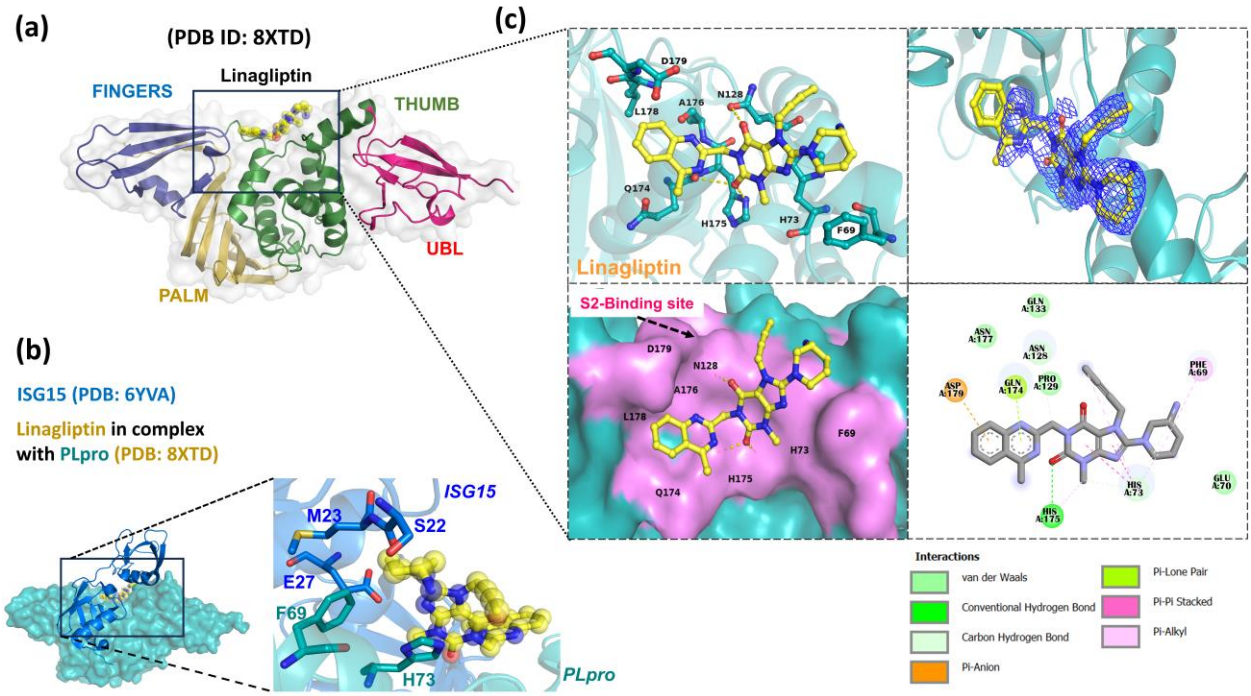

Figure 6: *(a) Crystal structure of SARS-CoV-2 PLpro in complex with identified compound Linagliptin (PDB ID: 8XTD) with PLpro shown as cartoon representation and the Linagliptin shown as yellow spheres. The identified compound Linagliptin binds at the S2-binding pocket. The thumb domain (residues 61-180) is colored as green (residues 61-180), the palm (residues 239-315) as yellow, the finger (residues 181-238), and the UBL domain (residues 1-60) as red. (b) Superimposition of the crystal structure of SARS-CoV-2 PLpro+Linagliptin (PDB ID: 8XTD) complex with crystal structure of SARS-CoV-2 PLproC111S in complex with mouse-ISG15 (PDB ID: 6YVA, ISG15 in blue cartoon). SARS-CoV-2 PLpro is depicted as teal green and the identified compound Linagliptin is represented as yellow spheres. (c) An enlarged view depicting intermolecular interactions of Linagliptin to the S2-binding pocket. The compound is shown as yellow sticks and the PLpro residues involved in binding are depicted as teal green sticks. Dashed yellow lines show hydrogen bonds. The electron density omit map (contour level = 3 σ) is shown as blue mesh. The 2-dimensional image for PLpro-Linagliptin interactions are prepared using Discovery Studio.*

To understand the molecular basis of SARS-CoV-2 PLpro inhibition by Lithocholic acid, we determined the X-ray crystal structure for protease co-crystallized with Lithocholic acid (PDB ID: 8X1X). The structure reveals electron density of Lithocholic acid occupying three binding sites on PLpro, including the substrate binding-cleft and the ISG15 S2-binding site (Figure 7). At the S2-binding pocket, Lithocholic acid I forms hydrophobic interactions with the side chains of Phe69, His73, Asn128, Gln174, His175, Ala176, Asn177, Leu178, and Asp179 (Figure 7). Interaction of Lithocholic acid I with the key natural substrate interacting residues of PLpro

(Phe69, His73, Asn128) reveals molecular basis of inhibition mechanism of PLpro by Lithocholic acid I, disrupting the PPI between PLpro and ISG15 or di-Ub (Figure 7). Superimposition of PLproC111S:Lithocholic acid I complex structure over SARS-CoV-2 PLpro:ISG15 structure suggests disruption of interactions between PLpro and ISG15. Remarkably, in the presence of Lithocholic acid I, the essential residues of ISG15, Ser22, Met23, Ser26, and K30, which are known to interact with the S2 pocket of PLpro, are no longer accessible to form contacts with PLpro (Figure 7). To our surprise, a second binding site for Lithocholic acid II was observed at a novel site near the zinc-finger motif (Figure 3.14). The interactions of inhibitor are stabilized by hydrophobic interactions with Tyr213, Lys217, Thr257, Tyr305, Lys306, Glu307, Asn308, and Ser309 (Figure 7). Additionally, Lithocholic acid II forms H-bond interaction with Glu214 further stabilizing the complex (Figure 7). In addition, a third molecule of Lithocholic acid III, occupies the substrate-binding cleft pocket forming interactions with Asn267 and Gln269, the two prime residues of the flexible BL2 loop.

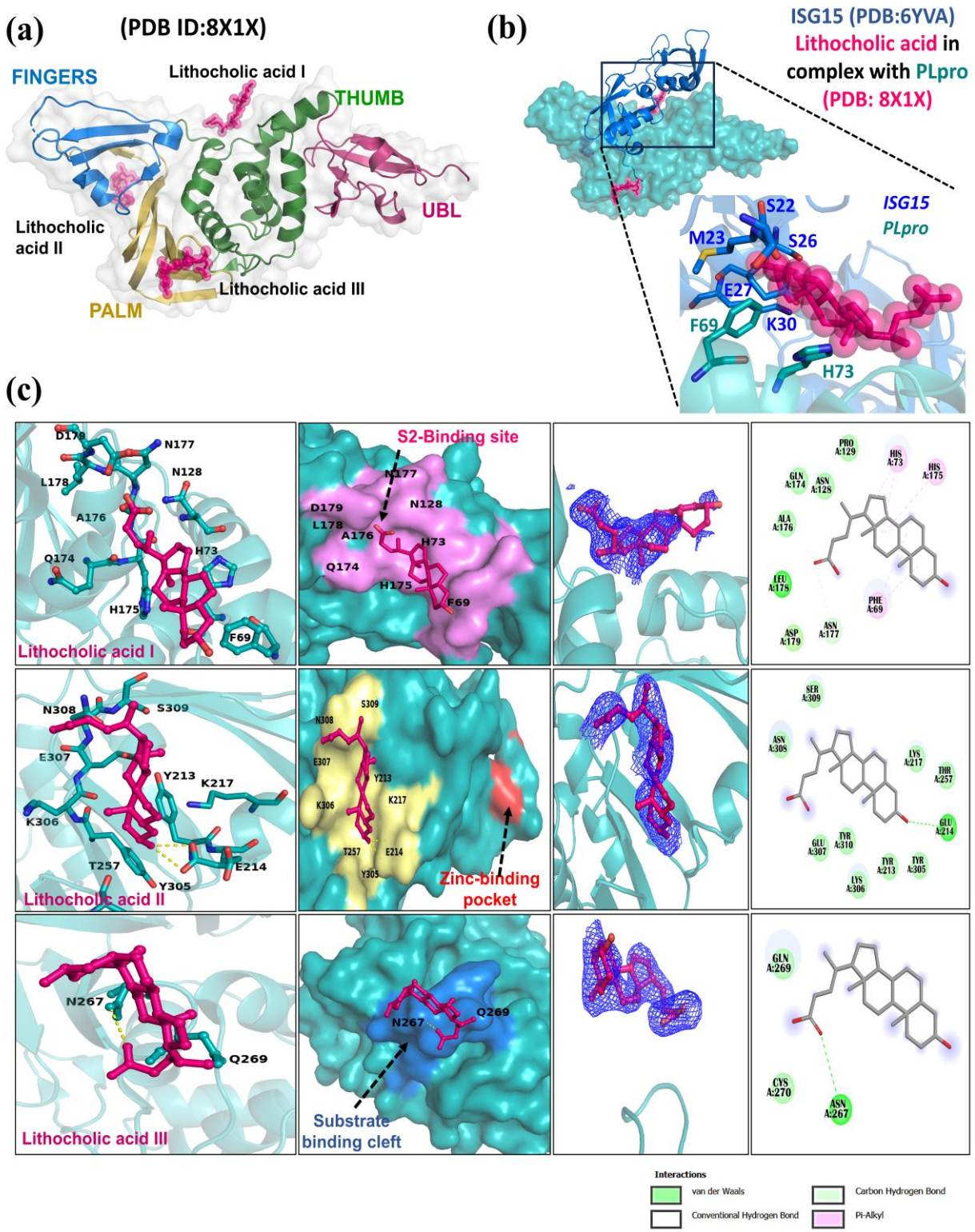

Figure 7: *(a) Crystal structure of SARS-CoV-2 C111S-PLpro in complex with identified compound Lithocholic acid with PLpro shown as cartoon representation and the Lithocholic acid shown as pink spheres. The identified compound binds at three sites: Lithocholic acid I (S2-*

binding site), II (a novel site near the zinc-binding pocket), and III (Substrate binding cleft). The thumb domain (residues 61-180) is colored as green (residues 61-180), the palm (residues 239-315) as yellow, the finger (residues 181-238), and the UBL domain (residues 1-60) as red. (b) Superimposition of the crystal structure of SARS-CoV-2 PLpro+Lithocholic acid complex with crystal structure of SARS-CoV-2 PLproC111S in complex with mouse-ISG15 (PDB ID: 6YVA, ISG15 in blue cartoon). SARS-CoV-2 PLpro is depicted as teal green surface and the identified compound Lithocholic acid is represented as pink spheres at three sites. (c) An enlarged view depicting intermolecular interactions of Lithocholic acid I to the S2-binding pocket, Lithocholic acid II to a novel site near the zinc-binding pocket, and Lithocholic acid III to substrate-binding pocket. The compound is shown as pink sticks and the PLpro residues involved in binding are depicted as teal green sticks. Dashed yellow lines show hydrogen bonds. The electron density omit map (contour level = 3 σ) is shown as blue mesh. The 2-dimensional images for PLpro-Lithocholic acid interaction are prepared using Discovery Studio.

Discussion:

The urgency of the COVID-19 pandemic and the recurring outbreaks by the variants of SARS-CoV-2 have heavily increased the challenges of curbing the pandemic of COVID-19. Therefore, there continues to be a need for preemptive strategies and drug modalities to treat COVID-19 and PLpro is considered a valuable target for it. Drug repurposing provides an alternative approach for quick identification of potential drugs to combat COVID-19, and targeting viral proteases offers additional advantages owing to their druggability and highly conserved substrate-binding pocket. Given that the substrate-binding pocket is highly similar among variants of SARS-CoV-2, the present study focused on identifying several bonafide inhibitors that might prove to be effective against different strains of SARS-CoV-2. In addition to the protease activity, PLpro possesses DUB and deISGylating activities as an evasion mechanism against the host antiviral immune response. Several host proteases, including USP2 and USP7 exhibit the same deconjugating activity and structural homology as host-encoded DUBs, marking their similarity as a noteworthy target to be explored.

Upon viral infection, type 1 interferons (IFN-α/β) produced by the immune cells of the host activate the production of ISG15. The upregulated ISG15 protein thereby conjugates with JAK, STAT, and IRF-3 through a process called ISGylation, all of which are key players of Type-1 elicited antiviral response of the host [80]. Activation of RIG-I-like receptors (RIG-I) and melanoma differentiation-associated protein 5 (MDA5) by ISGylation also leads to establishment of an antiviral state in host cell. To evade host immunity, PLpro antagonizes ISG15 dependent activation of MDA5 and RIG1 protein through its DUB activity [81]. A dysregulated interferon mediated antiviral response could lead to pro-inflammatory cytokine storm in the COVID-19 patients, a major cause of mortalities among infected patients [81]. Thus, targeting PLpro might

serve as a dual target that could avert SARS-CoV-2 infection either by inhibition of its proteolytic activity or by upregulation of innate immune response [82].

In light of previous studies, we sought to determine whether an inhibitor of DUBs could potentially be active against PLpro. For this purpose, a structural alignment of PLpro with USP2 and USP7 was done. The structural comparison revealed a very less percentage of conservation among the three selected DUBs. However, the structurally conserved active site fold and orientation of catalytic triad residues Cys-His-Asp/Asn provided a hint to repurpose available USP inhibitors against PLpro of SARS-CoV-2 (Figure 1). Encouraged by structural and functional similarities among these DUBs, an *in-house* library of DUB and cyanopyrrolidine-ring inhibitors was constituted. A total of five compounds were finally selected after comprehensive virtual screening, docking study, and MD simulation studies (Table 1, Supplementary table 1, and Figure 1). The enzymatic assays, SPR binding kinetic studies, and *in vitro* studies against SARS-CoV-2 show that lithocholic acid, linagliptin, teneligliptin, and flupenthixol hold tremendous promise as a target to generate new class of antivirals against PLpro (Figures 2, 3, and 4). Each of these compounds displayed biochemical inhibition of PLpro and also inhibited the virus and significantly reduced the infectious virus titer in cell-based assays (Figures 2, 3, and 4). Concentration-dependent reduction in viral copy number (Figure 3 and 4) and infectious viral titer (supplementary figure 5) well below their cytotoxic concentration highlights the effective anti-SARS-CoV-2 activity of compounds in the present study. Dose-titration data depicts that nearly all (3 out of 4) tested compounds significantly inhibited replication of SARS-CoV-2 in one or both of these cell lines at potencies equivalent to or greater than those that was observed in case of Vero cells. Linagliptin displayed improved inhibitory effects in A549-ACE2 and HEK293T-ACE2 cells with EC_{50} value of 0.24 and 7.4, respectively, and was therefore continued further with *in vivo* validation studies (Figure 4). Interestingly, ligand-binding experiments using SPR were in line with the enzymatic inhibition and cell-based studies with observed K_D values in the micromolar range (lithocholic acid-PLpro: 79.3 μM; linagliptin-PLpro: 72.6 μM; flupenthixol-PLpro: 258.1 μM) (Figures 2). Though teneligliptin failed to discern binding with PLpro in SPR assay, its antiviral data suggested significant inhibitory effect against SARS-CoV-2, proposing a hint for other possible off-targets that could be explored (Figures 2, 3, and 4). The cytotoxicity profile in Vero cells, HEK293T-ACE2, and A549-ACE2 showed a CC_{50} value of > 50 μM marking them safe for use (Supplementary figure 4). Structural analysis revealed that both Linagliptin and Lithocholic acid occupied the S2-binding pocket of PLpro at the thumb domain, located at the interface between PLpro and ISG15 (Figure 6 and Figure 7). Once Linagliptin or Lithocholic acid occupies the S2 interface between PLpro and ISG15 substrate, it is likely to disrupt the interaction between PLpro and natural substrates such as ISG15 or di-Ub and therefore is presumed to upregulate the innate immune response of the host. Furthermore, altering the properties of S2 site with Linagliptin or Lithocholic acid offers potential to downregulate the deubiquitinase activity of coronaviral PLpro, thereby providing a novel strategy for structure based inhibition of SARS-CoV-2 and its emerging variants.

Previous studies on lithocholic acid report it to be a potent inhibitor of intestinal inflammatory responses [83]. In another study, lithocholic acid is reported to exert antiviral action on replication of porcine delta coronavirus replication (PDCoV) [84]. Recent clinical and experimental data on COVID-19 provides evidence for reduced mortality in infected patients with or without type 2 diabetes, after the use of gliptins (e.g., sitagliptin, alogliptin, etc.). Gliptins, a class of DPP4 inhibitors, antagonize SARS-CoV-2 virulence either by enhancing GLP-1 anti-inflammatory activity or by reducing overproduction of cytokines and downregulating the activity of macrophages [85][86]. These classes of inhibitors may halt the disease progression to a hyperinflammatory state after viral infection [87]. Flupenthixol, an anti-depressant and antipsychotic drug, is reported to significantly inhibit the entry of SARS-CoV and MERS [88].

In conclusion, the compounds identified in this study offer new perspectives for treatment of COVID-19. However, the need for clinical studies cannot be ruled out to validate these *in vitro* findings. Because PLpro is a highly conserved protein among coronaviruses, these top leads appear as strong therapeutic candidates against the SARS-CoV-2 infection or its emerging variants.

Acknowledgement:

This research was funded by Science and Engineering Research Board, Department of Science & Technology, the Government of India (Proj. ref no. IPA/2020/000054). S.C. and A.K thank the Council of Scientific & Industrial Research (CSIR), Government of India for financial support. S.N. acknowledges the Ministry of Human Resource Development, (MHRD), and R.R thank University Grants Commission (UGC), Government of India for research fellowship. A.S thank Prime Minister's Research Fellows (PMRF), MHRD for research fellowship. The authors acknowledge and thank the Macromolecular Crystallographic Facility (MCU) at IIC, Indian Institute of Technology, Roorkee.

References:

[1] R. E. Baker, S. W. Park, C. E. Wagner, and C. J. E. Metcalf, 'The limits of SARS-CoV-2 predictability', *Nat Ecol Evol*, vol. 5, no. 8, pp. 1052–1054, 2021, doi: 10.1038/s41559-021-01514-z.

[2] R. Mudgal, S. Nehul, and S. Tomar, 'Prospects for mucosal vaccine: shutting the door on SARS-CoV-2', *Hum Vaccin Immunother*, vol. 16, no. 12, pp. 2921–2931, Dec. 2020, doi: 10.1080/21645515.2020.1805992.

[3] T. Crellen *et al.*, 'Dynamics of SARS-CoV-2 with waning immunity in the UK population', *Philosophical Transactions of the Royal Society B: Biological Sciences*, vol. 376, no. 1829, p. 20200274, Jul. 2021, doi: 10.1098/rstb.2020.0274.

[4] E. Dolgin, 'COVID vaccine immunity is waning-how much does that matter?', *Nature*, vol. 597, no. 7878, pp. 606–607, 2021.

[5] C. Giannitsarou, S. Kissler, and F. Toxvaerd, 'Waning Immunity and the Second Wave: Some Projections for SARS-CoV-2', *Am Econ Rev Insights*, vol. 3, no. 3, pp. 321–338, 2021, doi: 10.1257/aeri.20200343.

[6] W. F. Garcia-Beltran *et al.*, 'Multiple SARS-CoV-2 variants escape neutralization by vaccine-induced humoral immunity', *Cell*, vol. 184, no. 9, pp. 2372-2383.e9, 2021, doi: https://doi.org/10.1016/j.cell.2021.03.013.

[7] Y. Weisblum *et al.*, 'Escape from neutralizing antibodies by SARS-CoV-2 spike protein variants', *Elife*, vol. 9, Oct. 2020, doi: 10.7554/eLife.61312.

[8] A. Dubey, S. Choudhary, P. Kumar, and S. Tomar, 'Emerging SARS-CoV-2 Variants: Genetic Variability and Clinical Implications', *Curr Microbiol*, vol. 79, no. 1, p. 20, 2021, doi: 10.1007/s00284-021-02724-1.

[9] H. Shan *et al.*, 'Development of potent and selective inhibitors targeting the papain-like protease of SARS-CoV-2', *Cell Chem Biol*, vol. 28, no. 6, pp. 855-865.e9, 2021, doi: https://doi.org/10.1016/j.chembiol.2021.04.020.

[10] G. Li and E. De Clercq, 'Therapeutic options for the 2019 novel coronavirus (2019-nCoV)', *Nature Reviews Drug Discovery 2021 19:3*, vol. 19, no. 3, pp. 149–150, Feb. 2020, doi: 10.1038/d41573-020-00016-0.

[11] R. Rani *et al.*, 'Multi-target direct-acting SARS-CoV-2 antivirals against the nucleotide-binding pockets of virus-specific proteins', *Virology*, vol. 577, pp. 1–15, 2022, doi: 10.1016/j.virol.2022.08.008.

[12] R. Rani, A. Singh, A. Pareek, and S. Tomar, 'In silico guided drug repurposing to combat SARS-CoV-2 by Targeting Mpro, the key virus specific protease', 2020.

[13] A. Schäfer *et al.*, 'Therapeutic efficacy of an oral nucleoside analog of remdesivir against SARS-CoV-2 pathogenesis in mice', *bioRxiv*, p. 2021.09.13.460111, Sep. 2021, doi: 10.1101/2021.09.13.460111.

[14] G. Kokic *et al.*, ‘Mechanism of SARS-CoV-2 polymerase stalling by remdesivir’, *Nat Commun*, vol. 12, no. 1, p. 279, 2021, doi: 10.1038/s41467-020-20542-0.

[15] J. Qiao *et al.*, ‘SARS-CoV-2 M(pro) inhibitors with antiviral activity in a transgenic mouse model’, *Science*, vol. 371, no. 6536, pp. 1374–1378, Mar. 2021, doi: 10.1126/science.abf1611.

[16] L. Zhang *et al.*, ‘Crystal structure of SARS-CoV-2 main protease provides a basis for design of improved α-ketoamide inhibitors’, *Science (1979)*, p. eabb3405, Mar. 2020, doi: 10.1126/science.abb3405.

[17] D. Wenhao *et al.*, ‘Structure-based design of antiviral drug candidates targeting the SARS-CoV-2 main protease’, *Science (1979)*, vol. 368, no. 6497, pp. 1331–1335, Jun. 2020, doi: 10.1126/science.abb4489.

[18] Y. Hu *et al.*, ‘Naturally Occurring Mutations of SARS-CoV-2 Main Protease Confer Drug Resistance to Nirmatrelvir’, *ACS Cent Sci*, vol. 9, no. 8, pp. 1658–1669, Aug. 2023, doi: 10.1021/acscentsci.3c00538.

[19] L. J. Stevens *et al.*, ‘Mutations in the SARS-CoV-2 RNA-dependent RNA polymerase confer resistance to remdesivir by distinct mechanisms’, *Sci Transl Med*, vol. 14, no. 656, p. eabo0718, Jun. 2024, doi: 10.1126/scitranslmed.abo0718.

[20] S. Iketani *et al.*, ‘Multiple pathways for SARS-CoV-2 resistance to nirmatrelvir’, *Nature*, vol. 613, no. 7944, pp. 558–564, 2023, doi: 10.1038/s41586-022-05514-2.

[21] Y. Hirotsu *et al.*, ‘Multidrug-resistant mutations to antiviral and antibody therapy in an immunocompromised patient infected with SARS-CoV-2’, *Med*, vol. 4, no. 11, pp. 813-824.e4, 2023, doi: https://doi.org/10.1016/j.medj.2023.08.001.

[22] Ma *et al.*, ‘Discovery of SARS-CoV-2 Papain-like Protease Inhibitors through a Combination of High-Throughput Screening and a FlipGFP-Based Reporter Assay’, *ACS Cent Sci*, vol. 7, no. 7, pp. 1245–1260, Jul. 2021, doi: 10.1021/acscentsci.1c00519.

[23] P. V’kovski, A. Kratzel, S. Steiner, H. Stalder, and V. Thiel, ‘Coronavirus biology and replication: implications for SARS-CoV-2’, *Nat Rev Microbiol*, vol. 19, no. 3, pp. 155–170, 2021, doi: 10.1038/s41579-020-00468-6.

[24] R. Arya *et al.*, ‘Structural insights into SARS-CoV-2 proteins’, *J Mol Biol*, vol. 433, no. 2, p. 166725, Jan. 2021, doi: 10.1016/j.jmb.2020.11.024.

[25] J. Osipiuk *et al.*, ‘Structure of papain-like protease from SARS-CoV-2 and its complexes with non-covalent inhibitors’, *Nat Commun*, vol. 12, no. 1, p. 743, 2021, doi: 10.1038/s41467-021-21060-3.

[26] P. Ren *et al.*, ‘A multi-targeting drug design strategy for identifying potent anti-SARS-CoV-2 inhibitors’, *Acta Pharmacol Sin*, 2021, doi: 10.1038/s41401-021-00668-7.

[27] Wong Jason and D. Blossom, ‘SARS-CoV-2 dependence on host pathways’, *Science (1979)*, vol. 371, no. 6532, pp. 884–885, Feb. 2021, doi: 10.1126/science.abg6837.

[28] R. Wioletta *et al.*, ‘Activity profiling and crystal structures of inhibitor-bound SARS-CoV-2 papain-like protease: A framework for anti–COVID-19 drug design’, *Sci Adv*, vol. 6, no. 42, p. eabd4596, Oct. 2021, doi: 10.1126/sciadv.abd4596.

[29] E. Weglarz-Tomczak, J. M. Tomczak, M. Talma, M. Burda-Grabowska, M. Giurg, and S. Brul, ‘Identification of ebselen and its analogues as potent covalent inhibitors of papain-like protease from SARS-CoV-2’, *Sci Rep*, vol. 11, no. 1, p. 3640, 2021, doi: 10.1038/s41598-021-83229-6.

[30] D. Shin *et al.*, ‘Papain-like protease regulates SARS-CoV-2 viral spread and innate immunity’, *Nature*, vol. 587, no. 7835, pp. 657–662, 2020, doi: 10.1038/s41586-020-2601-5.

[31] C. B. McClain and N. Vabret, ‘SARS-CoV-2: the many pros of targeting PLpro’, *Signal Transduct Target Ther*, vol. 5, no. 1, p. 223, 2020, doi: 10.1038/s41392-020-00335-z.

[32] Z. Shen *et al.*, ‘Potent, Novel SARS-CoV-2 PLpro Inhibitors Block Viral Replication in Monkey and Human Cell Cultures’, *bioRxiv*, p. 2021.02.13.431008, Jan. 2021, doi: 10.1101/2021.02.13.431008.

[33] Z. Fu *et al.*, ‘The complex structure of GRL0617 and SARS-CoV-2 PLpro reveals a hot spot for antiviral drug discovery’, *Nat Commun*, vol. 12, no. 1, p. 488, 2021, doi: 10.1038/s41467-020-20718-8.

[34] R. Kiira *et al.*, ‘A noncovalent class of papain-like protease/deubiquitinase inhibitors blocks SARS virus replication’, *Proceedings of the National Academy of Sciences*, vol. 105, no. 42, pp. 16119–16124, Oct. 2008, doi: 10.1073/pnas.0805240105.

[35] S. Patchett *et al.*, ‘A molecular sensor determines the ubiquitin substrate specificity of SARS-CoV-2 papain-like protease’, *Cell Rep*, vol. 36, no. 13, p. 109754, 2021, doi: https://doi.org/10.1016/j.celrep.2021.109754.

[36] Z. Fu *et al.*, ‘The complex structure of GRL0617 and SARS-CoV-2 PLpro reveals a hot spot for antiviral drug discovery’, *Nat Commun*, vol. 12, no. 1, p. 488, 2021.

[37] T. Klemm *et al.*, ‘Mechanism and inhibition of the papain-like protease, PLpro, of SARS-CoV-2’, *EMBO J*, vol. 39, no. 18, p. e106275, Sep. 2020, doi: 10.15252/embj.2020106275.

[38] X. Gao *et al.*, ‘Crystal structure of SARS-CoV-2 papain-like protease’, *Acta Pharm Sin B*, vol. 11, no. 1, pp. 237–245, 2021, doi: https://doi.org/10.1016/j.apsb.2020.08.014.

[39] C.-Y. Chou *et al.*, ‘Thiopurine analogues inhibit papain-like protease of severe acute respiratory syndrome coronavirus’, *Biochem Pharmacol*, vol. 75, no. 8, pp. 1601–1609, 2008, doi: https://doi.org/10.1016/j.bcp.2008.01.005.

[40] X. Chen, C.-Y. Chou, and G.-G. Chang, ‘Thiopurine Analogue Inhibitors of Severe Acute Respiratory Syndrome-Coronavirus Papain-Like Protease, a Deubiquitinating and deISGylating Enzyme’, *Antivir Chem Chemother*, vol. 19, no. 4, pp. 151–156, Feb. 2009, doi: 10.1177/095632020901900402.

[41] K.-W. Cheng *et al.*, ‘Thiopurine analogs and mycophenolic acid synergistically inhibit the papain-like protease of Middle East respiratory syndrome coronavirus’, *Antiviral Res*, vol. 115, pp. 9–16, 2015, doi: https://doi.org/10.1016/j.antiviral.2014.12.011.

[42] C. Bashore *et al.*, ‘Cyanopyrrolidine Inhibitors of Ubiquitin Specific Protease 7 Mediate Desulfhydration of the Active-Site Cysteine’, *ACS Chem Biol*, vol. 15, no. 6, pp. 1392–1400, Jun. 2020, doi: 10.1021/acschembio.0c00031.

[43] P. Jadav *et al.*, ‘Long-acting peptidomimetics based DPP-IV inhibitors’, *Bioorg Med Chem Lett*, vol. 22, no. 10, pp. 3516–3521, 2012, doi: https://doi.org/10.1016/j.bmcl.2012.03.078.

[44] E. Z. Fisman and A. Tenenbaum, ‘Antidiabetic treatment with gliptins: focus on cardiovascular effects and outcomes’, *Cardiovasc Diabetol*, vol. 14, no. 1, p. 129, 2015, doi: 10.1186/s12933-015-0294-0.

[45] D. Pitocco, L. Tartaglione, L. Viti, M. Di Leo, A. Pontecorvi, and S. Caputo, ‘SARS-CoV-2 and DPP4 inhibition: Is it time to pray for Janus Bifrons?’, *Diabetes Res Clin Pract*, vol. 163, p. 108162, May 2020, doi: 10.1016/j.diabres.2020.108162.

[46] Y. Yang, Z. Cai, and J. Zhang, ‘DPP-4 inhibitors may improve the mortality of coronavirus disease 2019: A meta-analysis’, *PLoS One*, vol. 16, no. 5, p. e0251916, May 2021, [Online]. Available: https://doi.org/10.1371/journal.pone.0251916

[47] T. Kawasaki, W. Chen, K. Tatsumi, and S. M. Dudek, ‘DPP4 Inhibition Attenuates LPS-Induced Lung Injury in Mice’, in *B27. The evil that endothelial cells do: implications for pulmonary vascular disease*, in American Thoracic Society International Conference Abstracts. , American Thoracic Society, 2018, pp. A2892–A2892. doi: doi:10.1164/ajrccm-conference.2018.197.1_MeetingAbstracts.A2892.

[48] I. Valencia, C. Peiró, Ó. Lorenzo, C. F. Sánchez-Ferrer, J. Eckel, and T. Romacho, ‘DPP4 and ACE2 in Diabetes and COVID-19: Therapeutic Targets for Cardiovascular Complications? ’, 2020. [Online]. Available: https://www.frontiersin.org/article/10.3389/fphar.2020.01161

[49] Z. Zong, Z. Zhang, L. Wu, L. Zhang, and F. Zhou, ‘The Functional Deubiquitinating Enzymes in Control of Innate Antiviral Immunity’, *Advanced Science*, vol. 8, no. 2, p. 2002484, Jan. 2021, doi: https://doi.org/10.1002/advs.202002484.

[50] P. Dhaka, A. Singh, S. Choudhary, P. Kumar, G. K. Sharma, and S. Tomar, ‘Discovery of anti-SARS-CoV-2 molecules using structure-assisted repurposing approach targeting N-protein’, *bioRxiv*, p. 2022.03.12.484092, Jan. 2022, doi: 10.1101/2022.03.12.484092.

[51] N. Murgolo *et al.*, ‘SARS-CoV-2 tropism, entry, replication, and propagation: Considerations for drug discovery and development’, *PLoS Pathog*, vol. 17, no. 2, pp. e1009225-, Feb. 2021, [Online]. Available: https://doi.org/10.1371/journal.ppat.1009225

[52] S. Choudhary *et al.*, ‘Unraveling antiviral efficacy of multifunctional immunomodulatory triterpenoids against SARS-COV-2 targeting main protease and papain-like protease’, *IUBMB Life*, vol. n/a, no. n/a, Dec. 2023, doi: https://doi.org/10.1002/iub.2793.

[53] E. Krissinel and K. Henrick, ‘Secondary-structure matching (SSM), a new tool for fast protein structure alignment in three dimensions’, *Acta Crystallogr D Biol Crystallogr*, vol. 60, no. 12 I, pp. 2256–2268, Dec. 2004, doi: 10.1107/S0907444904026460.

[54] H. M. Berman *et al.*, ‘The Protein Data Bank’, *Nucleic Acids Res*, vol. 28, no. 1, pp. 235–242, Jan. 2000, doi: 10.1093/nar/28.1.235.

[55] Schrodinger LLC, ‘The PyMOL Molecular Graphics System, Version 1.8’, 2015.

[56] X. Robert and P. Gouet, ‘Deciphering key features in protein structures with the new ENDscript server’, *Nucleic Acids Res*, vol. 42, no. W1, pp. W320–W324, Jul. 2014, doi: 10.1093/nar/gku316.

[57] O. Trott and A. J. Olson, 'AutoDock Vina: improving the speed and accuracy of docking with a new scoring function, efficient optimization, and multithreading', *J Comput Chem*, vol. 31, no. 2, pp. 455–461, Jan. 2010, doi: 10.1002/jcc.21334.

[58] N. M. O'Boyle, M. Banck, C. A. James, C. Morley, T. Vandermeersch, and G. R. Hutchison, 'Open Babel: An open chemical toolbox', *J Cheminform*, vol. 3, no. 1, p. 33, 2011, doi: 10.1186/1758-2946-3-33.

[59] S. Dallakyan and A. J. Olson, 'Small-molecule library screening by docking with PyRx', *Methods in Molecular Biology*, vol. 1263, pp. 243–250, 2015, doi: 10.1007/978-1-4939-2269-7_19.

[60] M. Rajat *et al.*, 'Selective Estrogen Receptor Modulators Limit Alphavirus Infection by Targeting the Viral Capping Enzyme nsP1', *Antimicrob Agents Chemother*, vol. 66, no. 3, pp. e01943-21, Jun. 2022, doi: 10.1128/aac.01943-21.

[61] L. J. Reed and H. Muench, 'A SIMPLE METHOD OF ESTIMATING FIFTY PER CENT ENDPOINT', *Am J Epidemiol*, vol. 27, no. 3, pp. 493–497, May 1938, doi: 10.1093/oxfordjournals.aje.a118408.

[62] L. G. Thorne *et al.*, 'Evolution of enhanced innate immune evasion by SARS-CoV-2', *Nature*, vol. 602, no. 7897, pp. 487–495, 2022, doi: 10.1038/s41586-021-04352-y.

[63] S. G. Devaraj *et al.*, 'Regulation of IRF-3-dependent Innate Immunity by the Papain-like Protease Domain of the Severe Acute Respiratory Syndrome Coronavirus', *Journal of Biological Chemistry*, vol. 282, no. 44, pp. 32208–32221, 2007, doi: https://doi.org/10.1074/jbc.M704870200.

[64] Shin *et al.*, 'Papain-like protease regulates SARS-CoV-2 viral spread and innate immunity', *Nature*, vol. 587, no. 7835, pp. 657–662, 2020, doi: 10.1038/s41586-020-2601-5.

[65] A. Pozhidaeva *et al.*, 'USP7-Specific Inhibitors Target and Modify the Enzyme's Active Site via Distinct Chemical Mechanisms', *Cell Chem Biol*, vol. 24, no. 12, pp. 1501-1512.e5, 2017, doi: https://doi.org/10.1016/j.chembiol.2017.09.004.

[66] I. E. Wertz and J. M. Murray, 'Structurally-defined deubiquitinase inhibitors provide opportunities to investigate disease mechanisms', *Drug Discov Today Technol*, vol. 31, pp. 109–123, 2019, doi: https://doi.org/10.1016/j.ddtec.2019.02.003.

[67] M. Renatus *et al.*, 'Structural Basis of Ubiquitin Recognition by the Deubiquitinating Protease USP2', *Structure*, vol. 14, no. 8, pp. 1293–1302, 2006, doi: https://doi.org/10.1016/j.str.2006.06.012.

[68] V. Srinivasan *et al.*, 'Antiviral activity of natural phenolic compounds in complex at an allosteric site of SARS-CoV-2 papain-like protease', *Commun Biol*, vol. 5, no. 1, p. 805, 2022, doi: 10.1038/s42003-022-03737-7.

[69] C.-C. Cho *et al.*, 'Drug Repurposing for the SARS-CoV-2 Papain-Like Protease', *ChemMedChem*, vol. 17, no. 1, p. e202100455, Jan. 2022, doi: https://doi.org/10.1002/cmdc.202100455.

[70] M. Hazra, 'Anti-Diabetic Prescriptions Evaluation for Metformin, Sitagliptin and Gemigliptin among Early Moderate Grade New Type II Diabetes Mellitus Patients in Global Tertiary Care

Hospitals: An Analytical Study in Rational Pharmacotherapeutics', Journal of Basic and Clinical Pharmacy.

[71] N. A. Alhakamy *et al.*, 'Evaluation of the Antiviral Activity of Sitagliptin-Glatiramer Acetate Nano-Conjugates against SARS-CoV-2 Virus', 2021. doi: 10.3390/ph14030178.

[72] A. Narayanan *et al.*, 'Identification of SARS-CoV-2 inhibitors targeting Mpro and PLpro using in-cell-protease assay', *Commun Biol*, vol. 5, no. 1, p. 169, 2022, doi: 10.1038/s42003-022-03090-9.

[73] S. B. Biering *et al.*, 'Screening a Library of FDA-Approved and Bioactive Compounds for Antiviral Activity against SARS-CoV-2', *ACS Infect Dis*, vol. 7, no. 8, pp. 2337–2351, Aug. 2021, doi: 10.1021/acsinfecdis.1c00017.

[74] L. Riva *et al.*, 'Discovery of SARS-CoV-2 antiviral drugs through large-scale compound repurposing', *Nature*, vol. 586, no. 7827, pp. 113–119, 2020, doi: 10.1038/s41586-020-2577-1.

[75] S. Yuan *et al.*, 'Targeting papain-like protease for broad-spectrum coronavirus inhibition', *Protein Cell*, vol. 13, no. 12, pp. 940–953, Dec. 2022, doi: 10.1007/s13238-022-00909-3.

[76] X. Chen, X. Yang, Y. Zheng, Y. Yang, Y. Xing, and Z. Chen, 'SARS coronavirus papain-like protease inhibits the type I interferon signaling pathway through interaction with the STING-TRAF3-TBK1 complex', *Protein Cell*, vol. 5, no. 5, pp. 369–381, May 2014, doi: 10.1007/s13238-014-0026-3.

[77] Cao, L. Duan, B. Huang, Y. Xiong, G. Zhang, and H. Huang, 'The SARS-CoV-2 papain-like protease suppresses type I interferon responses by deubiquitinating STING', *Sci Signal*, vol. 16, no. 783, p. eadd0082, Jul. 2023, doi: 10.1126/scisignal.add0082.

[78] M. Békés, G. J. van der Heden van Noort, R. Ekkebus, H. Ovaa, T. T. Huang, and C. D. Lima, 'Recognition of Lys48-Linked Di-ubiquitin and Deubiquitinating Activities of the SARS Coronavirus Papain-like Protease', *Mol Cell*, vol. 62, no. 4, pp. 572–585, 2016, doi: https://doi.org/10.1016/j.molcel.2016.04.016.

[79] P. M. Wydorski *et al.*, 'Dual domain recognition determines SARS-CoV-2 PLpro selectivity for human ISG15 and K48-linked di-ubiquitin', *Nat Commun*, vol. 14, no. 1, p. 2366, 2023, doi: 10.1038/s41467-023-38031-5.

[80] D. S. M. Lewis *et al.*, 'Aloin isoforms (A and B) selectively inhibits proteolytic and deubiquitinating activity of papain like protease (PLpro) of SARS-CoV-2 in vitro', *Sci Rep*, vol. 12, no. 1, p. 2145, 2022, doi: 10.1038/s41598-022-06104-y.

[81] G. Liu *et al.*, 'ISG15-dependent activation of the sensor MDA5 is antagonized by the SARS-CoV-2 papain-like protease to evade host innate immunity', *Nat Microbiol*, vol. 6, no. 4, pp. 467–478, 2021, doi: 10.1038/s41564-021-00884-1.

[82] S. Choudhary *et al.*, 'Unraveling antiviral efficacy of multifunctional immunomodulatory triterpenoids against SARS-COV-2 targeting virus-specific enzymes', *bioRxiv*, p. 2023.06.24.546363, Jan. 2023, doi: 10.1101/2023.06.24.546363.

[83] J. B. J. Ward *et al.*, 'Ursodeoxycholic acid and lithocholic acid exert anti-inflammatory actions in the colon', *American Journal of Physiology-Gastrointestinal and Liver Physiology*, vol. 312, no. 6, pp. G550–G558, Mar. 2017, doi: 10.1152/ajpgi.00256.2016.

[84] F. Kong, X. Niu, M. Liu, and Q. Wang, ‘Bile acids LCA and CDCA inhibited porcine deltacoronavirus replication in vitro’, *Vet Microbiol*, vol. 257, p. 109097, 2021, doi: https://doi.org/10.1016/j.vetmic.2021.109097.

[85] R. Strollo and P. Pozzilli, ‘DPP4 inhibition: Preventing SARS-CoV-2 infection and/or progression of COVID-19?’, *Diabetes Metab Res Rev*, vol. 36, no. 8, p. e3330, Nov. 2020, doi: https://doi.org/10.1002/dmrr.3330.

[86] S. B. Solerte, A. Di Sabatino, M. Galli, and P. Fiorina, ‘Dipeptidyl peptidase-4 (DPP4) inhibition in COVID-19’, *Acta Diabetol*, vol. 57, no. 7, pp. 779–783, 2020, doi: 10.1007/s00592-020-01539-z.

[87] G. Iacobellis, ‘COVID-19 and diabetes: Can DPP4 inhibition play a role?’, *Diabetes Res Clin Pract*, vol. 162, Apr. 2020, doi: 10.1016/j.diabres.2020.108125.

[88] S. M. Fred *et al.*, ‘Antidepressant and Antipsychotic Drugs Reduce Viral Infection by SARS-CoV-2 and Fluoxetine Shows Antiviral Activity Against the Novel Variants in vitro ’, 2022.